

Improvement in Radar Precipitation

D.T1.1.3





Title of deliverable: D.T1.1.3 Improvement in Radar Precipitation

Authors:

Aart Overeem

Tim Vlemmix

Frans van Wijngaarden

Tiemo Mathijssen

Mats Veldhuizen

Ben Lankamp

Mando de Jong

Hidde Leijnse

Royal Netherlands Meteorological Institute (KNMI), De Bilt, the Netherlands

31 October 2023

The EMfloodResilience project is being carried out within the context of Interreg V-A Euregio MeuseRhine and is 90% funded from the European Regional Development Fund.

Management summary

Ground-based weather radar precipitation products are important for many applications, such as (flash flood) early warnings, climate monitoring, and water management. Radar products are employed as input for short-term weather predictions, so-called nowcasts. These products were also highly relevant for the extreme rainfall and associated flooding that occurred mid-July 2021 in the Belgian-Dutch-German border region. National meteorological services are responsible for maintaining radars and developing nationwide precipitation products and nowcasts. Many sources of error can influence the quality of radar products, and hence, nowcasts.

This report is the deliverable D.T1.1.3 “Improvement in radar precipitation” of the Interreg project EM-floodResilience (<https://emfloodresilience.eu/>) and addresses three corrections to further improve the reliability of radar precipitation products:

- Design and apply corrections for partial blockage of the radar beam (Chapter 1).
- Automatic correction for the electronic calibration of the radar (Chapter 2).
- Design and apply corrections for attenuation by a layer of water on the sphere protecting the radar antenna (Chapter 3).

Chapters 1, 2 and 3 provide a description of the respective problems with a literature overview, a description of the employed datasets, and an assessment of the performance of the tested detection and correction methods. Recommendations are provided for further research and possible implementation of the tested correction algorithms in operational radar precipitation products. Specifically, expected quality improvements in KNMI’s operational quantitative precipitation products are discussed, colloquially labelled as International Radar Composite (IRC) for external users, e.g., in water management.

In Chapter 1, the issue of beam blockage of radar signals is addressed. Obstacles, such as buildings, trees and hills, can partially block the radar signals from especially the lowest elevation scan. This can lead to a severe reduction in precipitation estimates at longer range from the radar, because it primarily depends on data from the lowest elevation scan. The issue of beam blockage is illustrated in Figure 1, where wind turbines in easterly direction cause a severe underestimation in the 6-month accumulation from one of KNMI’s radar precipitation products. In this chapter, beam-blockage analyses are provided employing digital elevation model data for all operational C-band radars in the Belgian-Dutch-German border region. Beam blockage can be severe. A correction for beam blockage is shown to be useful for the KNMI radar in Herwijnen, but also reveals that more research is needed to further reduce the influence of beam blockage on precipitation estimates. Finally, a tool has been developed to locate obstacles causing beam blockage.

Chapter 2 addresses two radar hardware calibration issues. The radar antenna pointing accuracy is relevant, because offsets in the antenna position will lead to deviations in the location of estimated precipitation with respect to its true location. Offsets in the received power by the radar can lead to under- or overestimation of precipitation. Solar monitoring is employed to estimate these offsets for

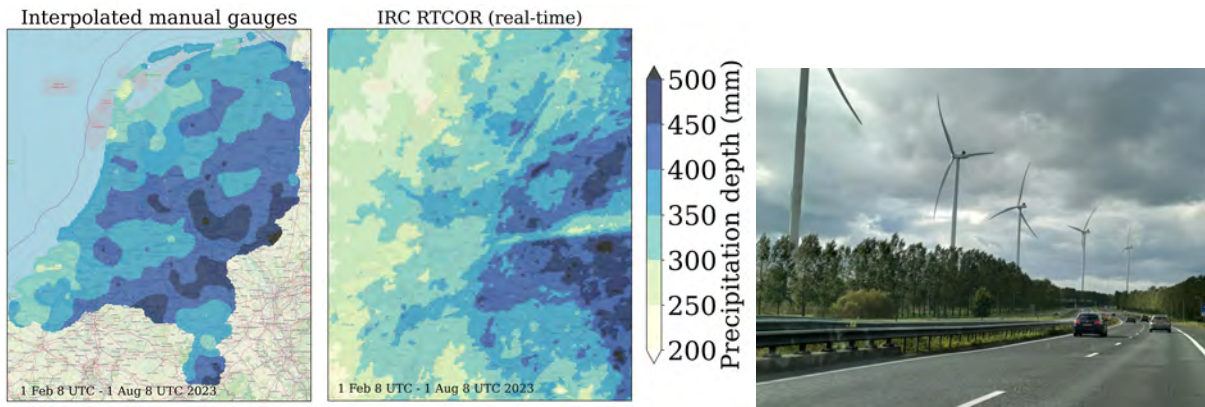


Figure 1: Six-monthly precipitation map for the Netherlands and surroundings for KNMI's interpolated manual rain gauge product (left) and for KNMI's real-time IRC product (middle). The underestimation in easterly direction as seen from the radar in Herwijnen in the middle of the Netherlands, is caused by a wind farm near motorway junction Deil (right). Map data ©OpenStreetMap contributors 2023. Distributed under the Open Data Commons Open Database License (ODbL) v1.0.

the two KNMI radars in the Netherlands. This requires so-called solar hits. An example of such a solar interference is shown in Figure 2 in easterly direction from the Den Helder radar in the northwest of the Netherlands. The methodology is extended to further remove outliers. Offsets are shown to be small for one of the radars. Offsets regarding the antenna position are also small for the radar closest to the Belgian-Dutch-German border region, but receiver offsets point to a severe underestimation. For the latter radar, results are not conclusive given the small number of data points, which requires further investigation.

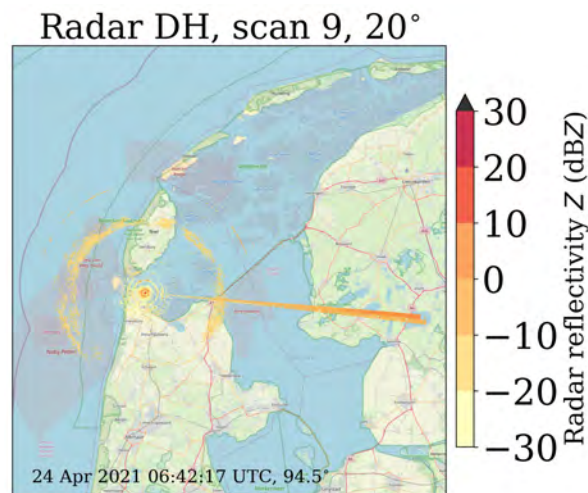


Figure 2: Illustration of a solar interference in polar radar data. Map of a domain around the KNMI radar in Den Helder, the Netherlands, with the radar reflectivity factor for the 20° elevation scan. Map data ©OpenStreetMap contributors 2023. Distributed under the Open Data Commons Open Database License (ODbL) v1.0.

In Chapter 3, the attenuation of radar signals due to a water layer at the protective cover of the radar, the radome, is investigated. Wet radome attenuation can lead to severe precipitation underestimation, as is illustrated in Figure 3, where the radar reflectivity factors strongly decrease between two consecutive time intervals. The impact of wet radome attenuation is investigated by checking whether a decrease in signal levels is found at the location of an obstacle nearby the radar site. These obstacles can give a high

and fairly constant reflectivity during dry weather. On average, a decrease in signal level is found when the radome can be considered wet, but such a decrease is not always present when the radome is wet. And signal levels can also decrease during dry conditions. This confirms that wet radome attenuation correction is a challenging topic, especially because of the irregular distribution of a water layer on the radome, e.g., caused by wind direction and wind speed. Recommendations are provided for future research.

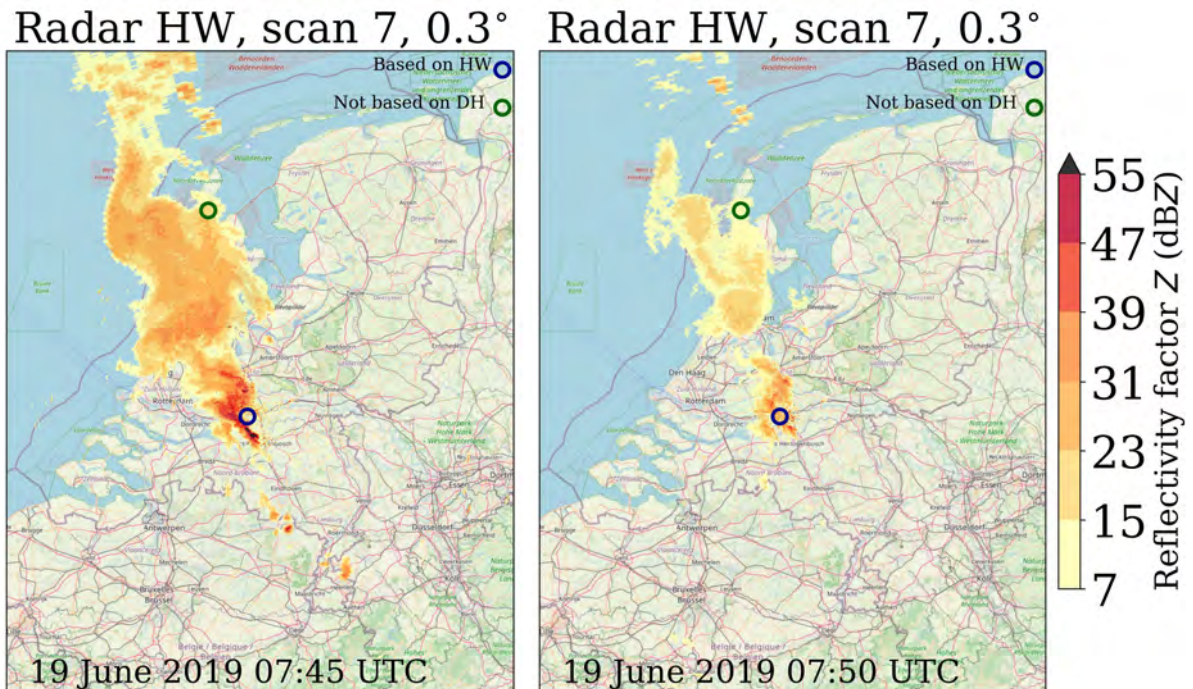



Figure 3: An illustration of the impact of wet radome attenuation on the radar reflectivity factor for the KNMI radar in Herwijnen. Map data ©OpenStreetMap contributors 2023. Distributed under the Open Data Commons Open Database License (ODbL) v1.0.

Contents

1	Design and apply corrections for partial beam blockage of the radar beam	8
1.1	Introduction to beam blockage	8
1.2	Digital elevation model data and beam-blockage computation	8
1.3	Method and Results	9
1.3.1	Beam blockage for KNMI radar Herwijnen	9
1.3.2	Precipitation estimation with beam-blockage correction for KNMI radar Herwijnen	11
1.3.3	Beam blockage for other Dutch, Belgian and German radars	13
1.3.4	Discussion	20
1.3.5	Beam blockage in KNMI's IRC products	21
1.4	Conclusions and recommendations	25
2	Automatic correction for the electronic calibration of the radar	27
2.1	Introduction to hardware calibration monitoring with the sun	27
2.2	Datasets & Methodology	28
2.2.1	Radar data	28
2.2.2	Solar flux monitoring station data	29
2.2.3	Algorithm	29
2.3	Results	33
2.3.1	Elevation and azimuth offsets	33
2.3.2	Receiver offsets	34
2.3.3	Discussion	34
2.4	Conclusions and recommendations	36



3	Design and apply corrections for attenuation by a layer of water on the sphere protecting the radar antenna	39
3.1	Introduction	39
3.2	Wet radome attenuation in the literature	41
3.3	Results	42
3.4	Conclusions and recommendations	45

Chapter 1

Design and apply corrections for partial beam blockage of the radar beam

1.1 Introduction to beam blockage

Weather radar beams can be blocked by obstacles in the vicinity of a radar, such as trees, buildings and wind turbines. This is called beam blockage or occultation. The radar beam can also be blocked by orography, even at longer range from a radar. Typically, only the lowest elevation scan(s) can be partially blocked by obstacles around the radar site. This can result in precipitation underestimation, especially at further range from the radar. There, the precipitation estimates are (mainly) retrieved from the lowest elevation scan data to measure as close to the Earth's surface as possible and to prevent overshooting of precipitation.

In case of partial beam-blockage, algorithms exist to assess the beam blockage and to compute a beam-blockage correction. Here, one method of beam-blockage detection is used to assess the beam-blockage fraction and correction for Belgian, Dutch and German weather radars. The effectiveness of the beam-blockage correction on precipitation estimates is evaluated for one Dutch radar over a 318-day dataset.

1.2 Digital elevation model data and beam-blockage computation

A common method for beam-blockage correction found in the scientific literature is to employ digital elevation model data (Bech et al., 2003; Krajewski et al., 2006; Bech et al., 2007; Lang et al., 2009; Cremonini et al., 2016). The cross section of the 3-dB radar beam of the lowest elevation scan with the surface can then be determined. The 3 dB-beam width contains most of the power of a radar beam, i.e., the part of the beam where it is at least 50% of the peak power at the centre of the beam. Its angular width is typically $\sim 1^\circ$. A radar measures in so-called range bins (voxels) with an angular resolution of $\sim 1^\circ$, an azimuth sector, and a radial resolution of a few hundred meters. Ideally, a Digital Surface Model (DSM) is used instead of a Digital Terrain Model (DTM), because it includes objects such as buildings and trees, and thus provides a more detailed perspective. The beam blockage fraction is computed for each range bin in all, typically 360, azimuth sectors of 1° . Different digital elevation models are used in this study:

- The Shuttle Radar Topography Mission (SRTM) with 30 m horizontal raster resolution (Farr and Kobrick, 2000; Farr and *et al.*, 2007; Kobrick, 2006; Rosen and *et al.*, 2000; NASA, 2013). A radar

system onboard the Space Shuttle Endeavour acquired the elevation data during an 11-day mission in February 2000. One GeoTIFF is obtained by selecting an area surrounding a radar at the OpenTopography portal¹

- For the Dutch KNMI radars in Den Helder and Herwijnen, the “Actueel Hoogtebestand Nederland version 4” (AHN4) is used as DSM². This is based on LiDAR observations taken from an airplane over the years 2020, 2021 and 2022. At least 95.4% of the points have a height accuracy of 15 cm³. It is more recent and has a much higher horizontal resolution of 0.5 m, 1 m, or 5 m compared to the SRTM dataset. Here, the 0.5 m dataset is used close to the radar sites and the 5 m product for a larger domain around the radar sites. Water is denoted as “no data”. GeoTIFF files are obtained for grid cells. These are subsequently merged into a mosaic GeoTIFF file that can be used for one radar site.

Version 1.19.2 of the open-source Python library wradlib (Heistermann et al., 2013; Mühlbauer et al., 2023) is used to compute the beam-blockage fraction and to visualise the digital elevation model height and the cumulative beam-blockage fraction. The intersection of the circular $\sim 1^\circ$ beam with the digital elevation model is computed to obtain the fraction of the beam that is blocked. The wradlib function “`qual.beam_block_frac`” (Wradlib, 2023b) employs the method of Bech et al. (2003), specifically Equation 2 and the Appendix. Next, the cumulative beam-blockage correction (CBBC; dB) is computed from the cumulative beam blockage fraction (CBBF) along the radar beam (Zhang et al., 2013):

$$\text{CBBC} = -10 \times \log_{10}(1 - \text{CBBF}). \quad (1.1)$$

1.3 Method and Results

The analyses focus on the KNMI radar in Herwijnen (Figure 1.1), for which pronounced underestimation due to beam blockage is known to be an issue, as has been noted by water authorities and an engineering company. For example, this is an issue for water balance studies on historical radar data. Hence, the beam-blockage computations and corrections have been extensively tested for this radar. First, beam blockage is evaluated and obstacles are identified. Second, a 318-day dataset from this radar is corrected for beam blockage. Precipitation estimates are evaluated by investigating radar-derived annual precipitation maps and by comparing with KNMI’s daily manual rain gauge accumulations. Third, beam blockage is investigated for three Belgian, one Dutch, and three German radars, including all operational C-band weather radars in the Interreg region of this project, the Belgian-Dutch-German border region. The locations of all the employed radars are provided in Figure 1.1. Fourth, the outcomes are discussed. Fifth, the impact of beam blockage on KNMI’s quantitative precipitation estimation products is investigated. Finally, conclusions and recommendations are provided.

1.3.1 Beam blockage for KNMI radar Herwijnen

For a domain close to the Herwijnen radar, the AHN4 0.5 m horizontal resolution DSM is employed. Figure 1.2 (top panel) shows the terrain height, computed beam-blockage fraction and correction factor for the lowest elevation scan (0.3°). Except for blockage in northeasterly direction (0.8 dB), beam blockage is negligible. This analysis suggests that trees and other obstacles within a few kilometres around the Herwijnen radar site do not pose a serious problem at this time. With a tool developed at KNMI,

¹<https://portal.opentopography.org/raster?opentopoID=OTSRTM.082015.4326.1>

²<https://www.ahn.nl/ahn-the-making-of/>; <https://www.arcgis.com/home/webmap/viewer.html?layers=77da2e9eeea8427aab2ac83b79097b1a>

³<https://www.ahn.nl/kwaliteitsbeschrijving>

Radar locations



Figure 1.1: The KNMI weather radar in Herwijnen, the Netherlands (left) and map with the locations of the weather radars for which beam blockage is computed (right). Map data ©OpenStreetMap contributors 2023. Distributed under the Open Data Commons Open Database License (ODbL) v1.0.

the beam blockage by specific obstacles around a radar site in the Netherlands can be computed and visualised for a chosen range bin. This is illustrated in Figure 1.3 for a range bin in northeasterly direction (31°) containing a group of trees resulting in partial beam blockage. Adjacent range bins are also affected by this or the slightly more northeasterly group of trees, i.e., multiple 1° azimuth sectors, but the beam blockage can be less severe.

Note that local obstacles, such as trees, would go unnoticed when using the native ~ 400 m radial resolution. Hence, the range bins are simulated with a ~ 5 m radial resolution to capture local obstacles as much as possible. Also note that the employed wradlib function only obtains the digital elevation model height from the centroid (middle) of the range bin, and does not average the elevation data over the entire range bin. Next, a much larger domain is considered using the AHN4 5 m horizontal resolution DSM (Figure 1.2, bottom panel). Again, range bins are simulated with a ~ 5 m radial resolution. Note that the correction is sometimes larger than the maximum value of the scale. This scale is chosen to emphasise the beam blockage by orography by the Utrecht Hill Ridge towards the northeast. In the direction of the Belgian-Dutch-German border region, mild beam blockage is present over a medium number of azimuth sectors. Figure 1.4 shows the altitude of the radar beam and the associated beam-blockage fraction as a function of range from the radar in the direction of the 69-m high peak of the Utrecht Hill Ridge (“Amerongse Berg”; excluding the height of vegetation). For AHN4, this peak is captured much better than when SRTM is used, with a beam-blockage fraction of ~ 0.1 and ~ 0.07 , respectively.

Next, the computed beam-blockage fractions from the 0.5 m & 5 m domains are summed for each simulated ~ 5 m range bin. From this, the cumulative beam-blockage correction is computed. The cumulative beam-blockage correction factors at the end of each native range bin are then assigned to each range bin at the native ~ 400 -m radial resolution. The cumulative beam-blockage fraction and correction at the native range bin resolution are shown in Figure 1.5. Now, this beam-blockage correction field can be used to correct for beam blockage. Note that the row of trees just north of the radar site (Figure 1.1) does not show up in the beam-blockage computations, but is expected to become a problem in the

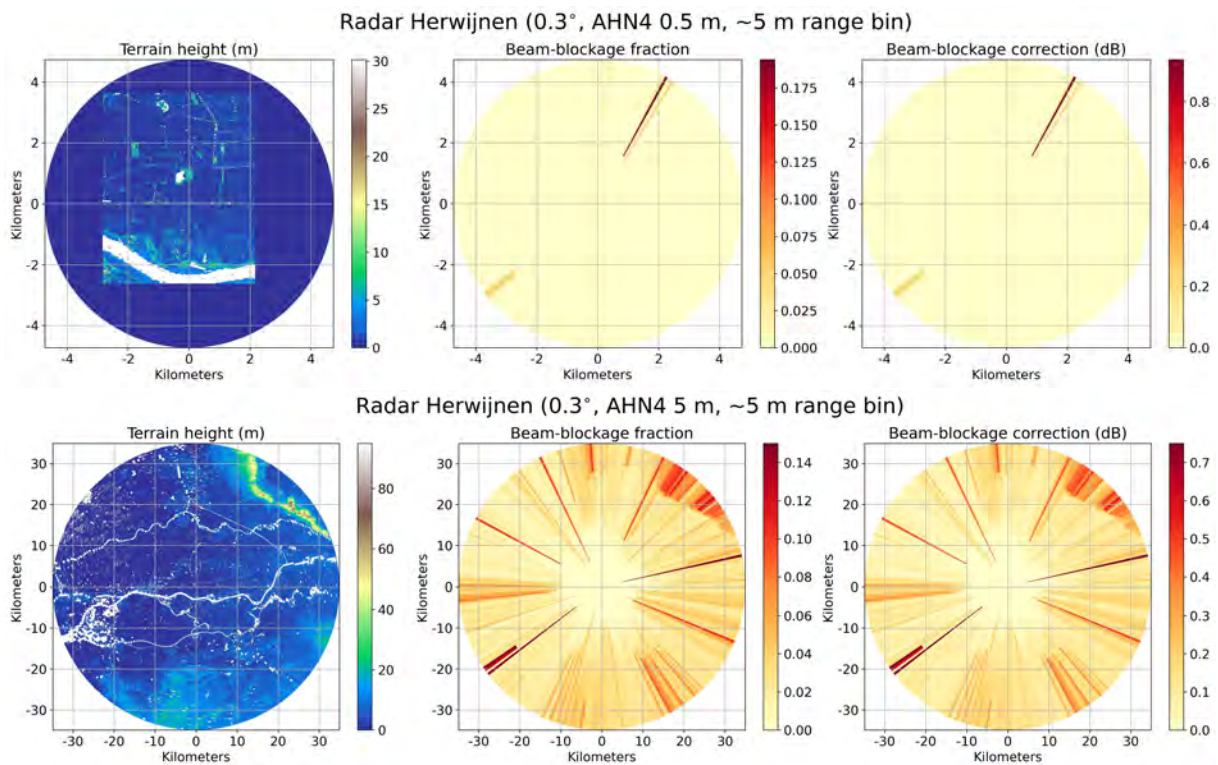


Figure 1.2: Height from AHN4 (left), computed cumulative beam-blockage fraction (middle) and correction (right) for a small (top panel) and large (bottom panel) domain around KNMI's Herwijnen radar site for the lowest elevation scan. For the bottom panel the fraction and correction is sometimes larger than the maximum value of the scale.

future when the trees will grow higher.

1.3.2 Precipitation estimation with beam-blockage correction for KNMI radar Herwijnen

The beam-blockage correction field from the previous section is applied to 5-min elevation scan data from the 0.3° scan number 7 from the Herwijnen radar for 318 days in the period August 2017 through July 2018. This implies that the correction field in dB is just added to the data field with (horizontally polarised) radar reflectivity factor values. The recipe from Overeem et al. (2021) is followed to obtain precipitation estimates. In summary, Doppler clutter filtering has been applied at the signal processor, fuzzy logic non-meteorological echo removal as described in Overeem et al. (2020) and rain-induced attenuation correction are applied to the data from scans 5 (2.0°), 6 (0.8°) and 7 (0.3°). Precipitation accumulations are obtained from the radar reflectivity factors by employing the Marshall-Palmer Z-R relationship $Z = 200 \times R^{1.6}$.

From the annual precipitation map, the impact by beam blockage becomes less apparent for the dataset where the beam-blockage correction has been applied, with substantial increases in the northeast of the Netherlands (top panel Figure 1.6). However, beam blockage is still quite severe, showing that it cannot be entirely removed by employing this method. By incorporating data from the KNMI radar in Den Helder (compositing), the impact of beam blockage in the northeast of the Netherlands is reduced, but this also reveals beam blockage for the Den Helder radar in southerly direction (bottom panel Figure 1.6). The accumulations based on Herwijnen only, are often much higher than those for the composite. One reason for this is melting precipitation in the so-called bright band (circular patterns), that is par-

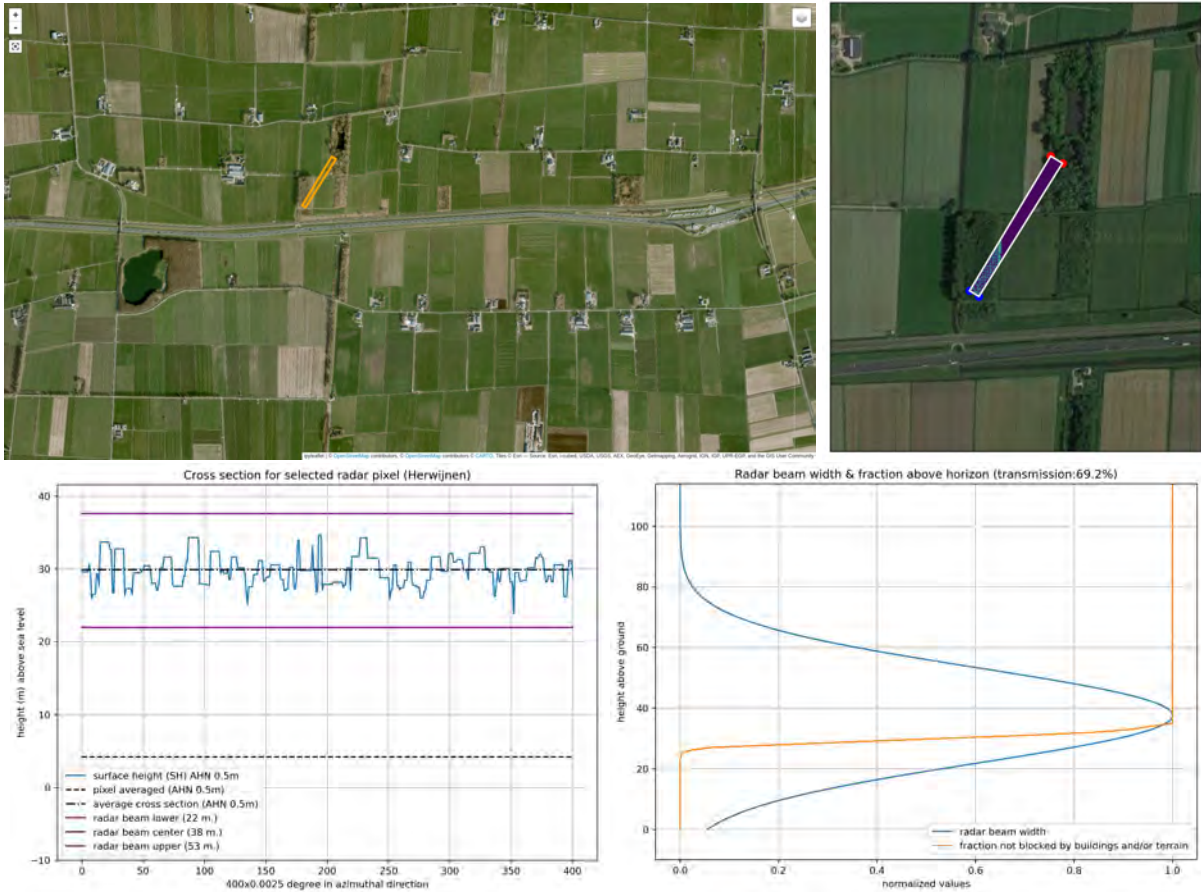


Figure 1.3: A group of trees ~ 1.8 km northeast of the Herwijnen radar, resulting in beam blockage. Based on AHN4. The transmission value is the part of the beam that is not blocked in this range bin.

tially averaged out in the composite (both radars will usually not experience the bright band at the same location due to the different range from the radars). The ratio of the beam-blockage corrected dataset with respect to the uncorrected dataset is also shown in Figure 1.6. In the Belgian-Dutch-German border region the ratio is between 1.03 and 1.06 for a larger area. Finally, a spatial verification of daily rainfall against KNMI's manual rain gauge network is provided in Figure 1.7. For most stations, a severe underestimation is found (left). The underestimation becomes less severe for the beam-blockage corrected dataset. Typically an increase of a few percentage point in the relative bias is obtained (right), as can be noted in the northeast of the Netherlands. Also in the south of the Dutch province of Limburg, the precipitation estimates improve for some rain gauge locations. The annual precipitation in the beam-blockage affected area in the northeast of the Netherlands seems tens of percent lower than that of adjacent azimuth sectors (Figure 1.6), suggesting that only part of the actual beam blockage is detected.

Note that the presented results are meant to show the effectiveness of a beam-blockage correction method, but are not representative for the quality of KNMI's gauge-adjusted radar precipitation products. One of the most important reasons is that no rain gauges have been used to adjust the radar data. Specifically, KNMI's IRC products have substantially improved since February 2023 by applying additional algorithms. Especially, the vertical profile of reflectivity correction helps to increase precipitation estimates at long range from radars.

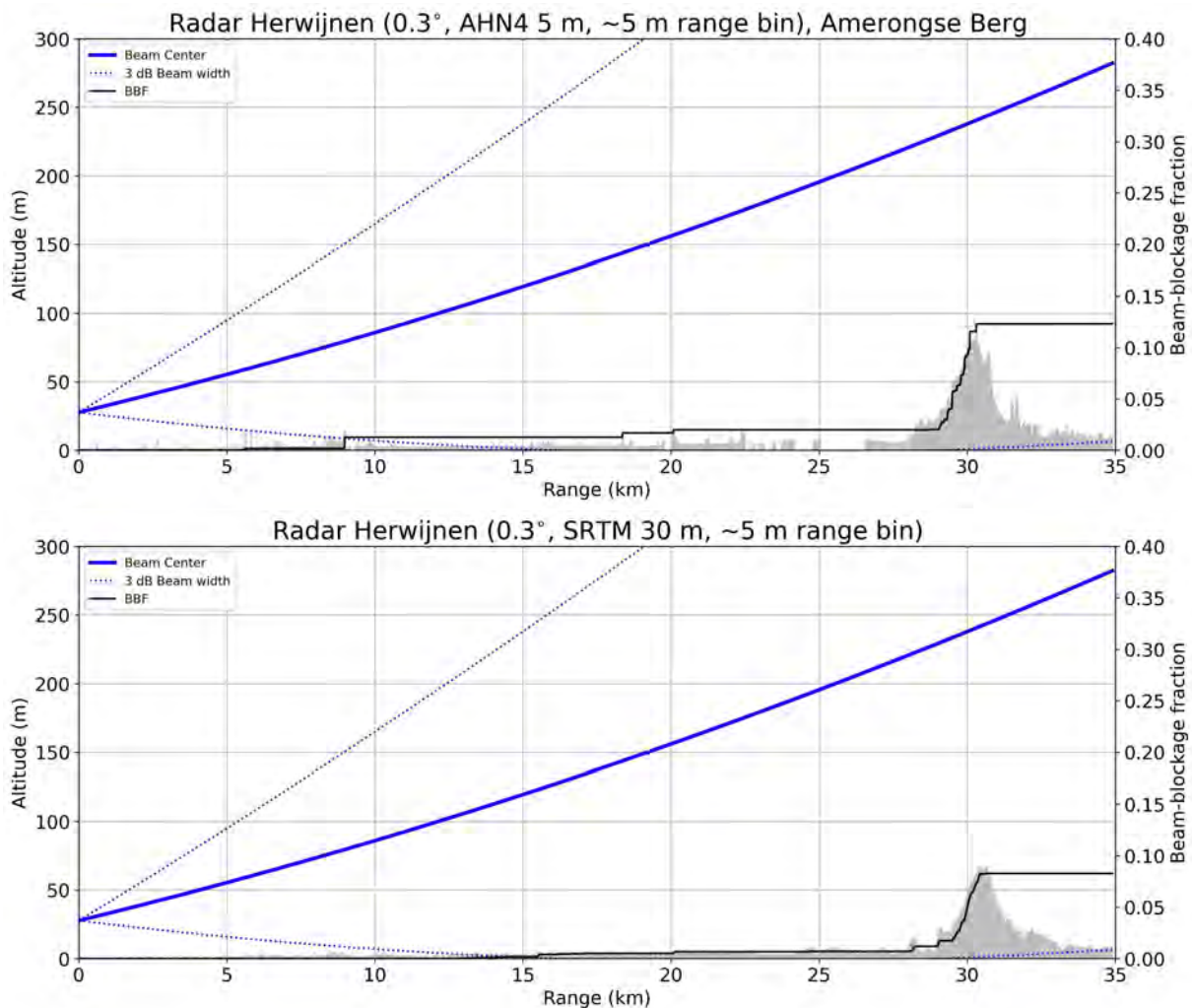


Figure 1.4: Altitude of the lowest elevation scan with respect to mean sea level as a function of range from the radar. The thick blue line denotes the centre of the radar beam, the dotted blue lines indicate the extent of the 1° beam. The gray-shaded areas denote obstacles, specifically around 30 km orography by the Utrecht Hill Ridge. The black line denotes the cumulative beam-blockage fraction encountered along the radar beam.

1.3.3 Beam blockage for other Dutch, Belgian and German radars

The KNMI radar in Den Helder is also evaluated, because KNMI noticed that also some beam blockage occurs for this radar. Moreover, other radars of interest for the Belgian-Dutch-German border region, are also evaluated: the VMM (Vlaamse Milieu Maatschappij) radar in Houthalen-Helchteren, the RMI (Royal Meteorological Institute) radars in Jabbeke and Wideumont, and the DWD (Deutscher Wetterdienst) radars in Essen and Neuheilenbach. These radars are also used in KNMI's IRC products, except for the one in Neuheilenbach. The latest addition to the KNMI IRC products, in August 2023, is the radar in Wideumont.

For the Den Helder radar, the beam-blockage fraction and correction analyses for the 5-m resolution AHN4 DSM (Figure 1.8, bottom panel), with simulated range bins with a 5-m radial resolution, only shows strong blockage in northerly direction (~ 3.0 dB) and very mild blockage due to dunes in southerly direction. The strong blockage in northerly direction is not revealed for the 0.5-m resolution AHN4 DSM (Figure 1.8, top panel), that reveals strong blockage in easterly directions. So, results from the 0.5-m and 5-m resolution AHN4 DSM are not consistent. This points to limitations of this approach within a

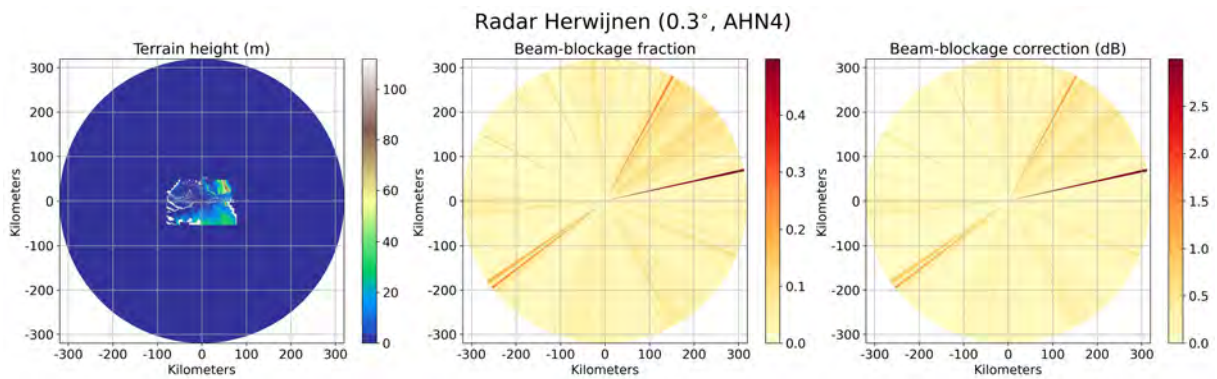


Figure 1.5: Height from AHN4 (left). Computed cumulative beam-blockage fraction (middle) and correction (right) for the radar domain of KNMI’s Herwijnen radar for the lowest elevation scan for the native ~ 400 -m radial resolution of the range bins. The correction field (right) can be applied to the radar reflectivity factor.

few kilometres of the radar site. Very local obstacles, such as nearby wind turbines and buildings at this naval base may complicate the computations. One idea to address this is to not use AHN data in very close proximity (tens of metres) to the radar site to avoid possible “beam blockage” by the radar tower itself, especially for the 0.5-m resolution AHN4, where the area with full blockage in easterly direction is suspicious. The influence on beam blockage by some local obstacles is further investigated in Figures 1.9 and 1.10. Given the many buildings and other obstacles around this radar site, it is difficult to find which obstacles are responsible for beam blockage. The source of strong blockage in northerly direction could not be found, only milder beam blockage. In contrast, for another azimuth sector, very strong blockage by a mast is found in northerly direction (Figure 1.9) with the KNMI tool, that is not captured by the beam-blockage analyses (Figure 1.8). Using a simulated range bin of 0.25 m in combination with the 0.5-m resolution AHN4, gives a different result (not shown), which confirms beam blockage in the direction of the mast. Going back to the results for the 5-m radial resolution, underestimation is found in southerly direction from the Den Helder radar in annual precipitation maps over a relatively narrow area (Figure 1.6, bottom panel). This beam blockage is known to be caused by two 45-m and 60-m high wind turbines from the Helsdeur wind farm with 44-m and 54-m diameter wicks, respectively⁴ located at 665 m and 781 m to the south of the Den Helder radar (Leijnse et al., 2022). The local analysis in Figure 1.10 confirms the impact of these wind turbines, but these are not present in the beam-blockage analyses in Figure 1.8.

For the radars in Belgium and Germany, the SRTM digital elevation model data are employed to estimate beam-blockage fraction and needed correction. Figure 1.11 provides the results for the lowest elevation scan for the radars in Essen, Neuheilenbach, Jabbeke, Wideumont, and Houthalen-Helchteren. For the Essen radar, a large region to the southeast is substantially affected (up to ~ 2.2 dB). For the Neuheilenbach radar, larger regions in the north and northeast are affected (up to ~ 0.75 dB) and a larger region in the northeast (up to ~ 1.8 dB). For the Jabbeke radar, a very large region to the south is affected, but blockage is relatively mild (up to ~ 0.5 dB). For the Wideumont radar, larger regions to the north are affected (up to ~ 0.5 dB). According to these analyses, beam blockage for the Belgian-Dutch-German border region is non-existent or small for these radars. In contrast, for the Houthalen-Helchteren radar, a large region to the southeast has beam blockage of ~ 1 to ~ 1.4 dB, covering the Belgian-Dutch-German border region. The beam blockage starts at the Ardennes (Figure 1.12).

⁴<https://www.atlasleefomgeving.nl/kaarten?config=3ef897de-127f-471a-959b-93b7597de188&activateOnStart=info,layermanager&gm-x=155000.00000000006&gm-y=416358.1266850175&gm-z=3.312315746690106&gm-b=1544180834512,true,1;1605001908247,true,1>

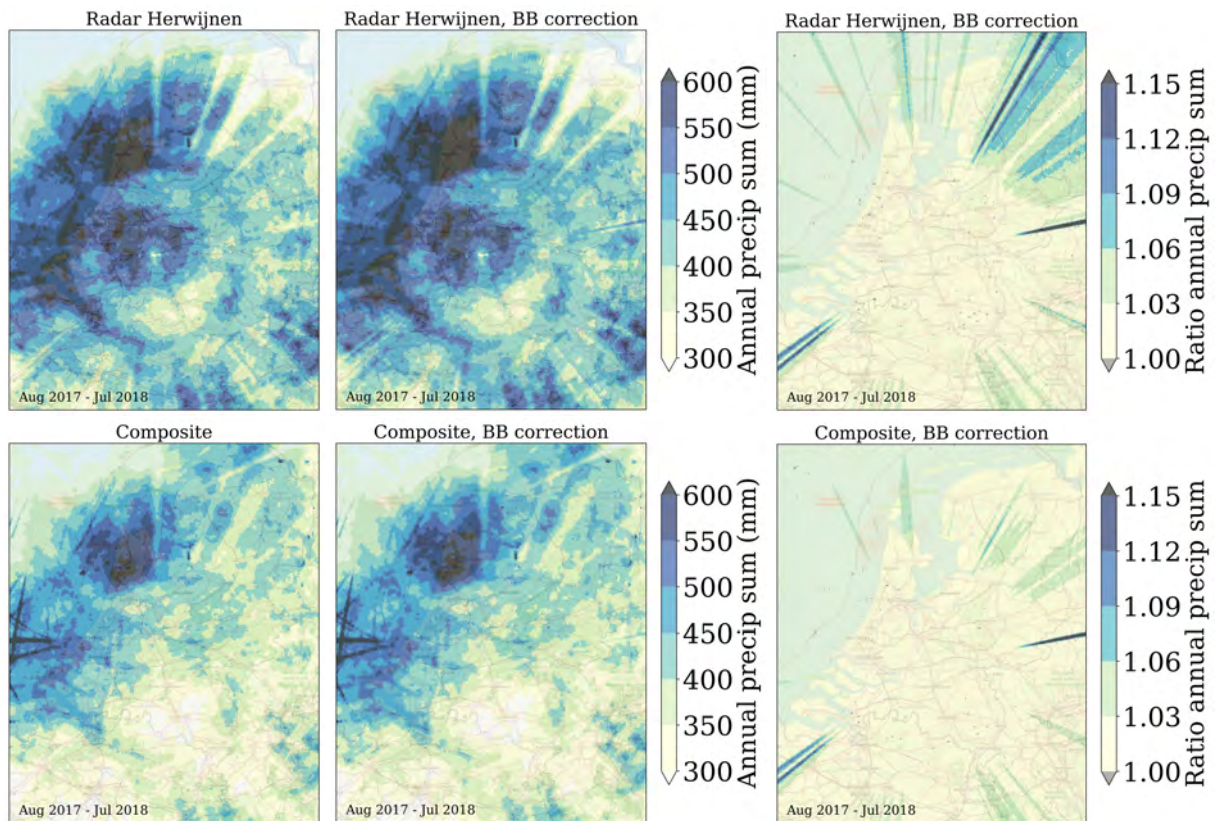


Figure 1.6: Annual precipitation map for the Netherlands and surroundings based on data from the KNMI radar in Herwijnen (top panel) and on data from the KNMI radars in Den Helder and Herwijnen (bottom panel). The maps in the middle show the effect of beam-blockage correction to the Herwijnen radar data. Ratio of annual precipitation for the beam-blockage corrected dataset with respect to the uncorrected dataset are shown on the right for the Herwijnen radar and the composite based on data from the Den Helder and Herwijnen radars. Map data ©OpenStreetMap contributors 2023. Distributed under the Open Data Commons Open Database License (ODbL) v1.0.

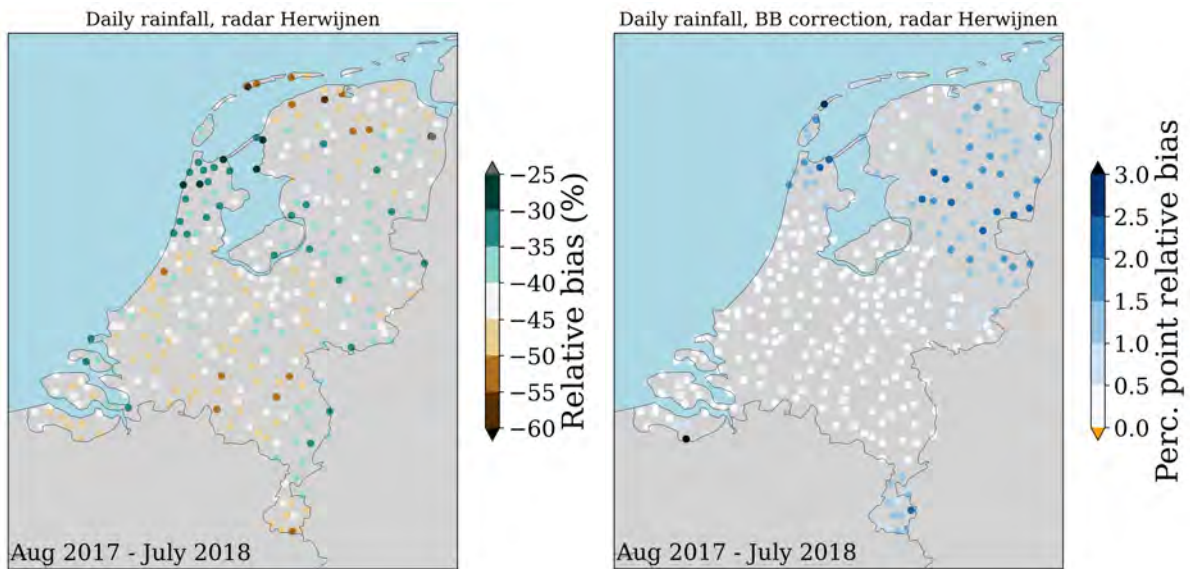


Figure 1.7: Spatial verification of radar daily precipitation accumulations against daily accumulations from KNMI's manual rain gauge network. The relative bias (left) is computed as the average of the residuals divided by the mean gauge rainfall accumulations. A residual is defined as the radar rainfall accumulation minus the gauge rainfall accumulation. The percentage point change in relative bias due to the beam-blockage correction is shown on the right. Map made with Natural Earth. Free vector and raster map data ©naturalearthdata.com.

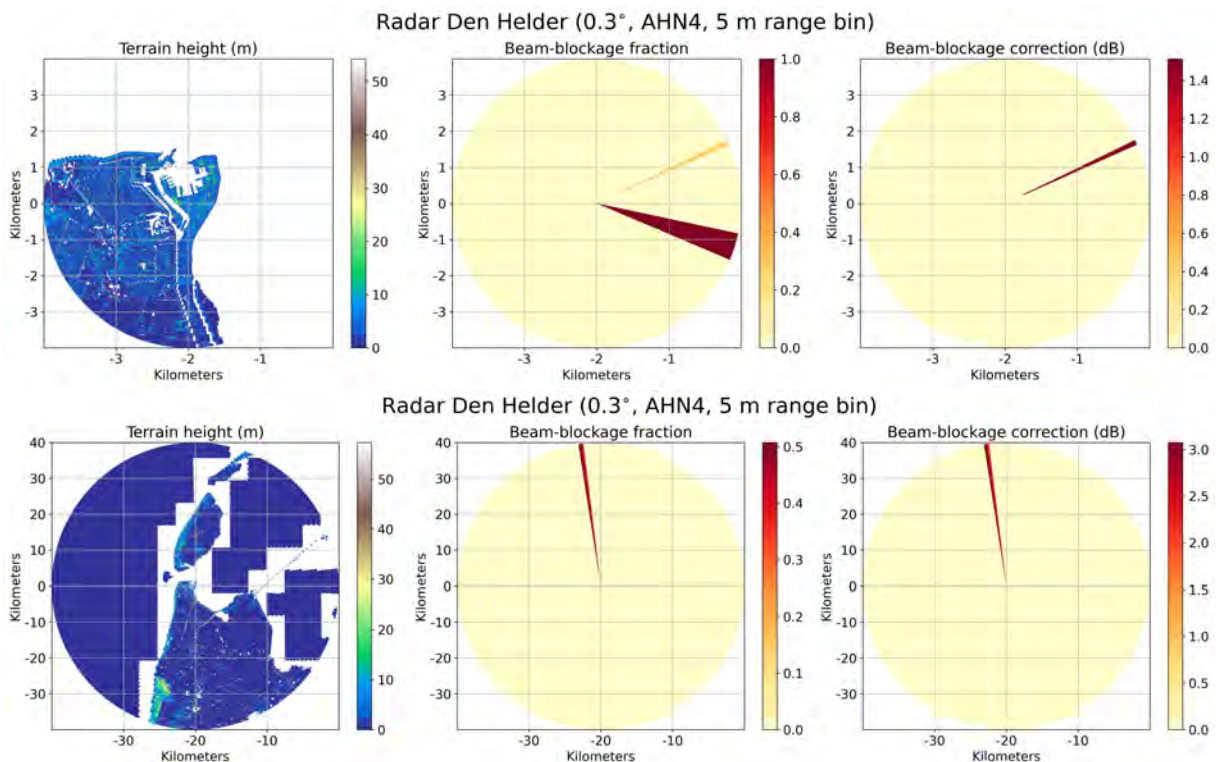


Figure 1.8: Height from AHN4 (left), computed cumulative beam-blockage fraction (middle) and correction (right) for a small (top panel) and large (bottom panel) domain around KNMI's Den Helder radar site for the lowest elevation scan.

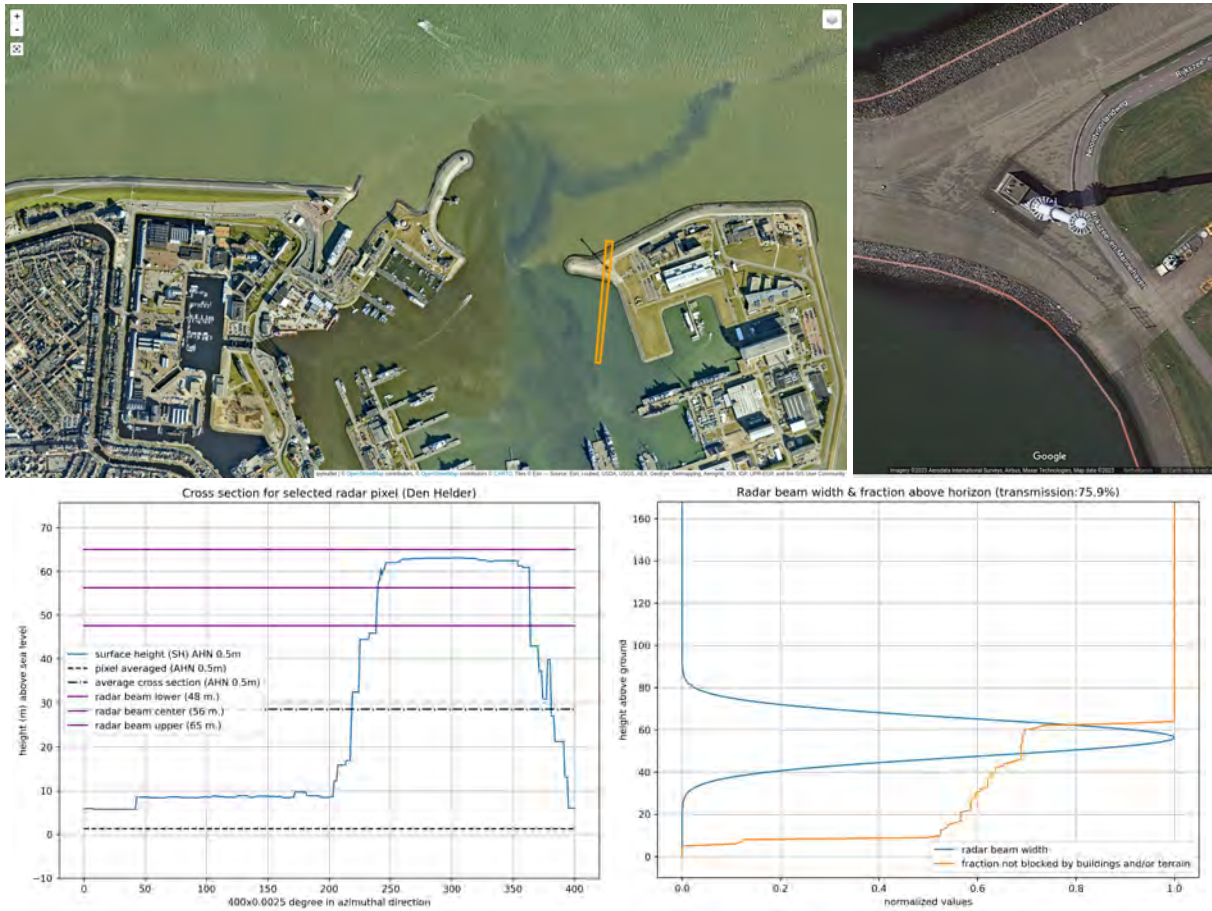


Figure 1.9: Effect of a mast at ~ 1.0 km distance in northerly direction (5°) of the Den Helder radar on beam blockage. Based on AHN4. The transmission value is the part of the beam that is not blocked in this range bin.

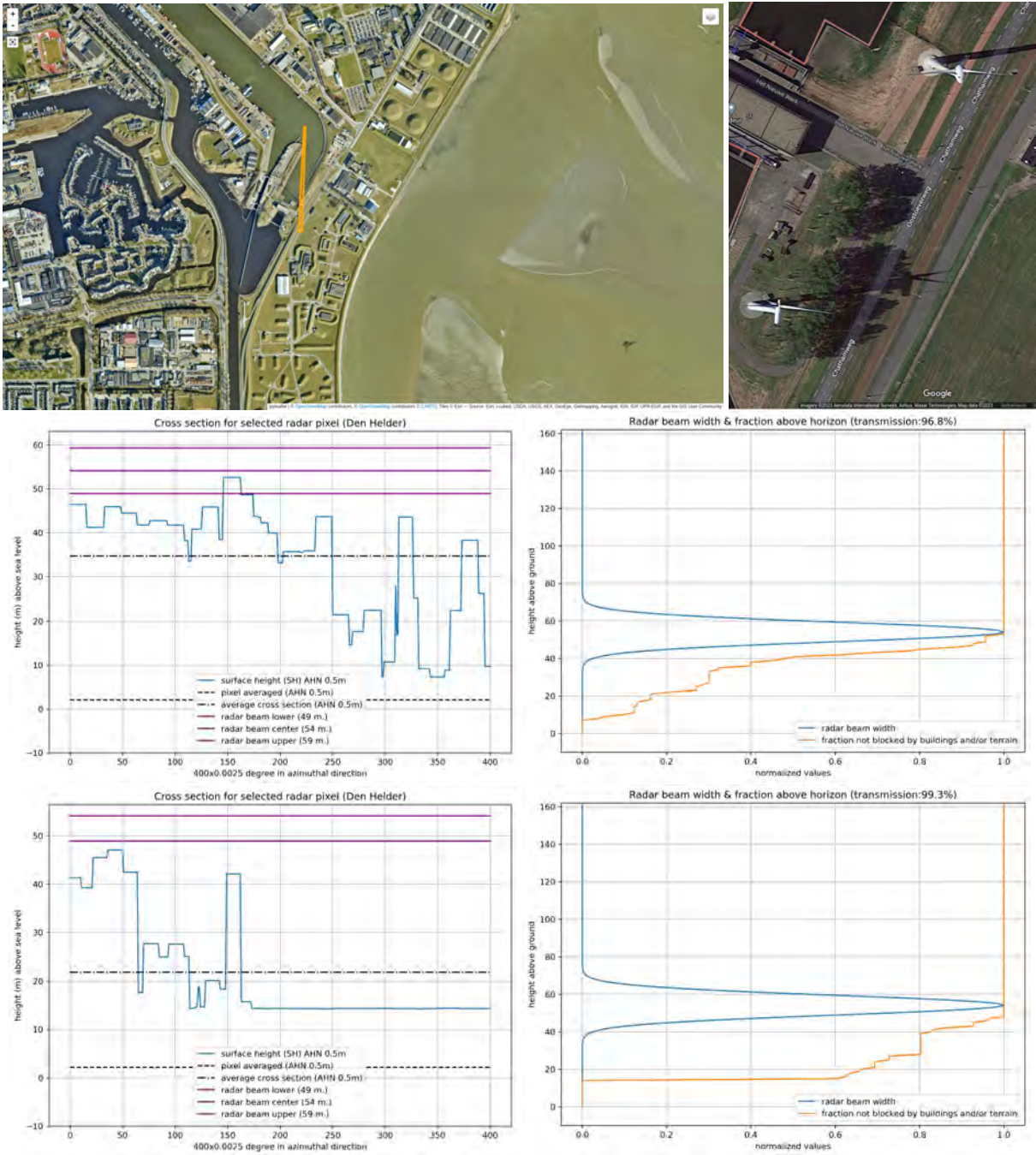


Figure 1.10: Effect of wind turbines at ~0.6 km distance in southerly direction (182° and 187°) of the Den Helder radar on beam blockage. Based on AHN4. The transmission value is the part of the beam that is not blocked in this range bin.

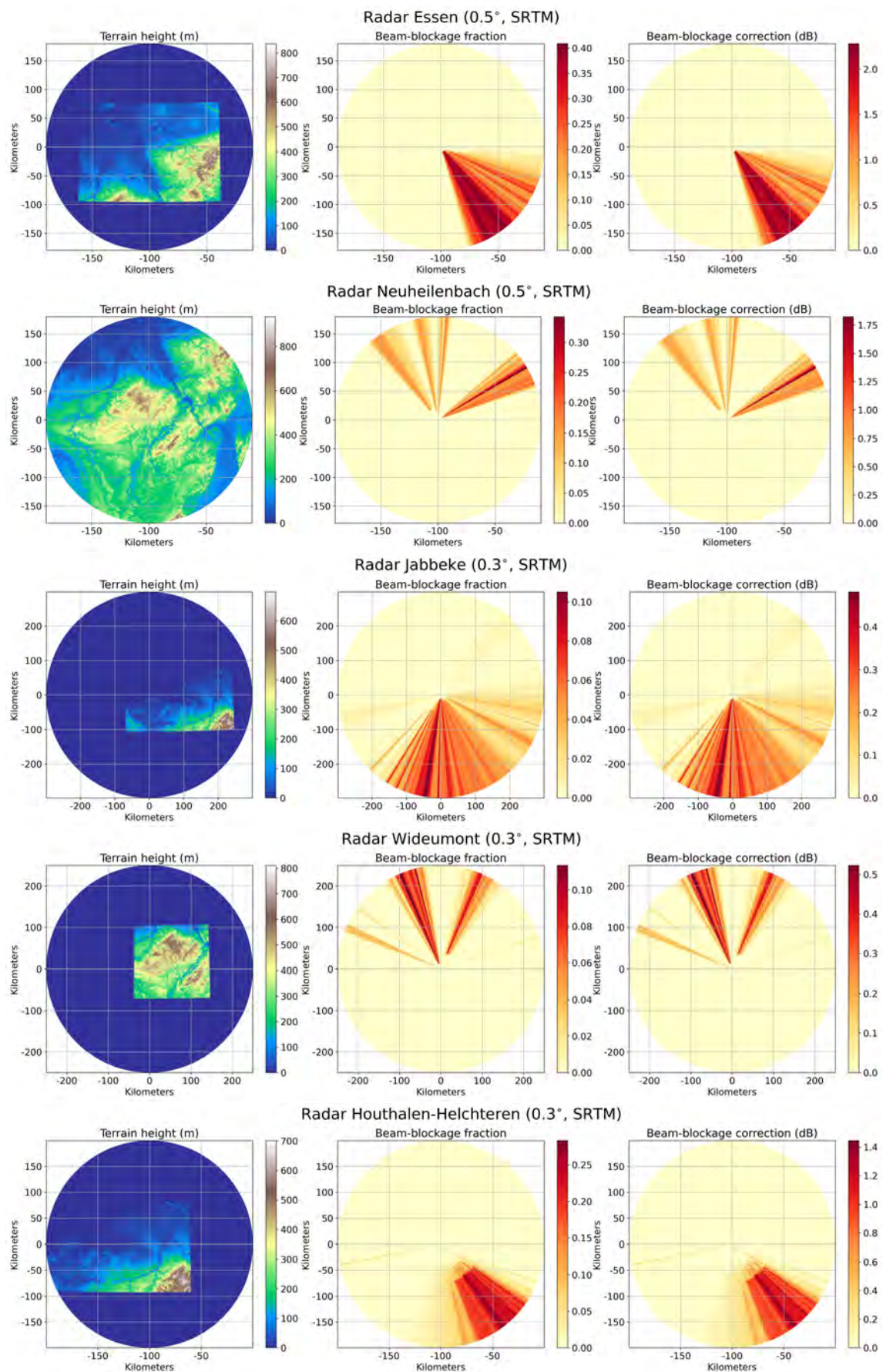


Figure 1.11: Height from SRTM (left), computed cumulative beam-blockage fraction (middle) and correction (right) employing the lowest elevation scan for a domain around two German and three Belgian radar sites relevant for the Belgian-Dutch-German border region.

Radar HH, scan 12, 0.3°

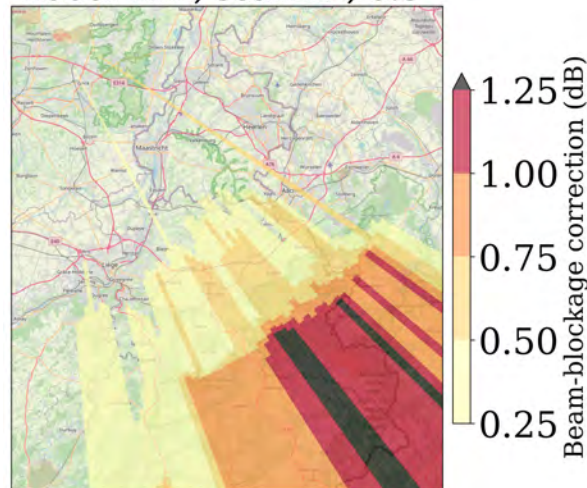


Figure 1.12: Computed cumulative beam-blockage correction for the VMM radar in Houthalen-Helchteren. Map data ©OpenStreetMap contributors 2023. Distributed under the Open Data Commons Open Database License (ODbL) v1.0.

1.3.4 Discussion

The beam-blockage correction only removes part of the underestimation induced by beam blockage. The most likely reasons for this are:

- Despite beam-blockage correction, the radar still does not sample the lowest part of the lowest elevation scan at longer range as it would when no beam blockage would occur.
- Normal propagation conditions are assumed in the analyses. In case of anomalous propagation due to temperature and moisture gradients in the atmosphere, refraction causes a larger part of the beam to reach the Earth's surface. Hence, a larger part of the beam can be blocked.

A less important reason is that only for beam blockage of the main lobe of the radar beam (3-dB beam width) is accounted for. Note that for all azimuth sectors, part of the 3-dB beam of a lowest elevation scan of 0.3° reaches the Earth's surface in normal propagation conditions within roughly 10–60 km of the radar, irrespective of beam blockage.

For the quantitative precipitation estimation with the Herwijnen radar data over the period August 2017 through July 2018, the beam-blockage correction field was obtained by employing AHN version 4. Figure 1.13 shows the collection years for AHN versions 3 and 4. AHN4 provides data for the years 2020, 2021, and 2022, that can include obstacles that are not yet present for the considered 318-day dataset. In Figure 1.6 some overestimation can be seen in easterly direction, because the Deil wind turbines did not exist in 2017 and 2018 yet. On the other hand, for AHN3, data for the area directly surrounding Herwijnen was already collected in 2015 and part of the province of Utrecht in the north was collected in 2014. Moreover, AHN4 is the most representative dataset for the present. Although beam-blockage computations have also been carried out with AHN3, it was decided to focus on AHN4. The period August 2017 through July 2018 was chosen because this has been used as a test dataset for all algorithms in KNMI's IRC product (e.g., Overeem et al. (2020, 2021)). This facilitates comparisons and the corresponding datasets are well known.



Figure 1.13: Collection years for AHN3 (left) and AHN4 (right). Figure taken from <https://www.ahn.nl/kwaliteitsbeschrijving>.

In the analyses, it is assumed that the radar antenna has a high pointing accuracy, i.e., low offset of the azimuth and elevation angle. For instance, if the antenna has a negative elevation angle offset, beam-blockage is more severe than computed. Hence, hardware calibration monitoring is important. This is addressed in Chapter 2 for another period than the periods considered in this chapter.

1.3.5 Beam blockage in KNMI's IRC products

In section 1.3.2, the beam-blockage correction has been applied to the data from KNMI's Herwijnen radar and has been evaluated on the radar accumulations from this radar and from a composite based on data from both KNMI radars. In KNMI's IRC products, also data from Belgian and German radars are incorporated. These products are currently the state-of-the-art for precipitation information for the Netherlands. Hence, it is relevant to investigate the occurrence of underestimation by beam blockage in the IRC products, which also gives information for all radars covering the Belgian-Dutch-German border region, except the Wideumont and Neuheilenbach radar. Three IRC products exist:

- Real-time 5-min accumulations (RTCOR⁵). Radar accumulations are adjusted with KNMI's automatic rain gauge accumulations (32 locations).
- Early reanalysis 5-min accumulations (RECOR⁶). For each day at 14:30 UTC, the RTCOR radar accumulations are adjusted with the available daily KNMI manual rain gauge accumulations (typically ~ 200 locations).
- Final reanalysis 5-min accumulations (RFCOR⁷). After a few weeks, the RTCOR radar accumulations are adjusted with the complete and validated daily KNMI manual rain gauge accumulations (319 locations).

⁵<https://dataplatform.knmi.nl/dataset/nl-rdr-data-rtcor-5m-tar-1-0>

⁶<https://dataplatform.knmi.nl/dataset/nl-rdr-data-recor-5m-1-0>

⁷<https://dataplatform.knmi.nl/dataset/nl-rdr-data-rfcor-5m-1-0>

Here, the 6-month precipitation accumulations over the period 1 February 8 UTC - 1 August 8 UTC are evaluated over the years 2022 and 2023 for the real-time and final reanalysis products. The 2022 period includes data from the Belgian radars from RMI in Jabbeke and VMM in Houthalen-Helchteren, as well as the German radar from DWD in Essen. The 2023 period also includes the German radar from DWD in Borkum. The quality of the IRC products has substantially improved since February 2023 by applying many additional algorithms to the radar data and by a spatial instead of mean-field bias adjustment with automatic rain gauge data. The real-time and final reanalysis products are evaluated in Figure 1.14. Indeed, the 2023 dataset shows a much better correspondence to KNMI's interpolated daily manual rain gauge accumulations⁸. Note that the rain gauges do only capture precipitation at their locations, whereas the radars provide full coverage with much higher spatial resolution.

A quantitative spatial evaluation is provided in Figure 1.15, where daily IRC real-time accumulations over the 6-month period are compared to KNMI's manual rain gauge accumulations. The overall quality improvement of the IRC product from 2023 compared to 2022 is strong, with much less spatial variability in relative bias for 2023. For the 2023 period, the underestimations in the northeast and especially in the east, close to the German border, are likely related to beam blockage. The Deil wind farm likely plays a large role in the latter. Many other locations reveal underestimations that cannot be easily related to beam blockage, though.

Further investigation of Figure 1.14 reveals that the underestimation due to beam blockage becomes less pronounced in the northeast of the Netherlands in the 2023 period. This is likely caused by the addition of the data from the Borkum radar, that is located northeast of this region. It can partly compensate for the underestimation due to its different viewpoint and relatively short distance to this region. In contrast, the underestimation in easterly direction seen from the Herwijnen radar has increased in 2023 compared to 2022. This can be related to beam blockage ~6 kilometres east of the Herwijnen radar, caused by a wind farm near motorway junction Deil. The strong computed beam blockage of almost 3 dB is based on AHN4 (Figure 1.5), that only contains 2 wind turbines. Currently, this wind farm Deil consists of 11 aligned wind turbines with a 140-m turbine height and 136-m diameter blades⁹. Figure 1.16 shows a satellite map with the locations of those wind turbines. For one wind turbine, the beam blockage is computed for one range bin showing that it is already substantial. The alignment of wind turbines is expected to substantially increase the blockage.

For the IRC product we recommend to:

- Implement the beam-blockage correction based on AHN4 for the Herwijnen radar. This is expected to partly compensate for beam blockage, especially in the northeast of the Netherlands and for the wind turbine induced blockage east of the radar in Herwijnen. Preferably, first evaluate this on the 6-month period from 2023, to investigate the effectiveness of beam-blockage correction. In addition, monitor beam blockage in the IRC product. Compare long-term accumulations before and after possible implementation of beam-blockage correction.
- Lower the quality index for regions subjected to beam blockage correction. When converting 3D to 2D data per radar, the beam-blockage affected lowest elevation scan then gets a lower weight. In addition, data from other radars will get a relatively large weight when combined with data from the Herwijnen radar. This is expected to result in lower underestimations in beam-blockage affected regions. Note that this will also result in a higher dependence on higher elevation data, which may result in underestimation. In general, this quality-based compositing would be recommendable for radar precipitation products.

⁸<https://dataplatform.knmi.nl/dataset/rd1-5>

⁹<https://www.atlasleefomgeving.nl/kaarten?config=3ef897de-127f-471a-959b-93b7597de188&activateOnStart=info,layermanager&gm-x=155000.00000000006&gm-y=416358.1266850175&gm-z=3.312315746690106&gm-b=1544180834512,true,1;1605001908247,true,1>

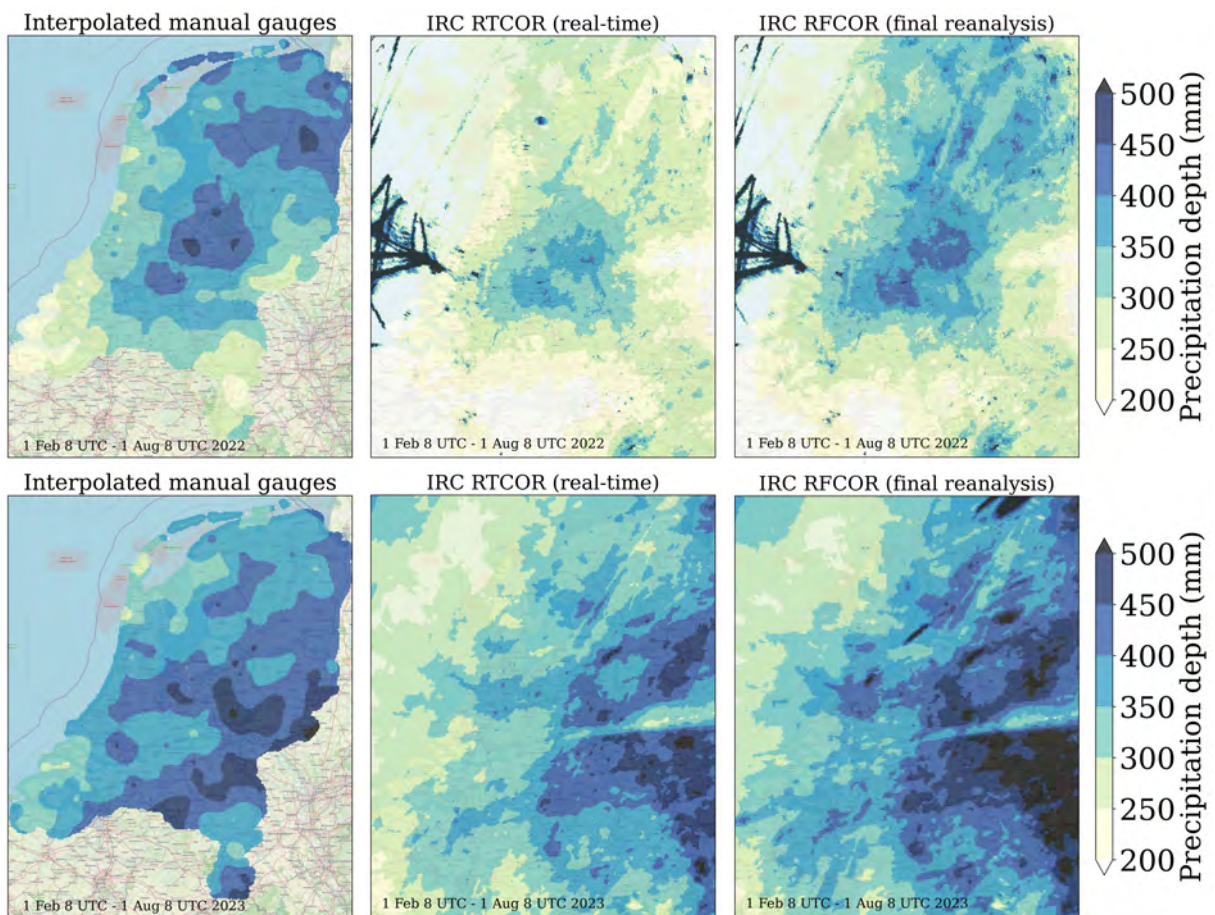


Figure 1.14: Six-monthly precipitation map for the Netherlands and surroundings for KNMI's interpolated manual rain gauge product (left), for KNMI's real-time (middle) and final reanalysis (right) IRC product. Map data ©OpenStreetMap contributors 2023. Distributed under the Open Data Commons Open Database License (ODbL) v1.0.

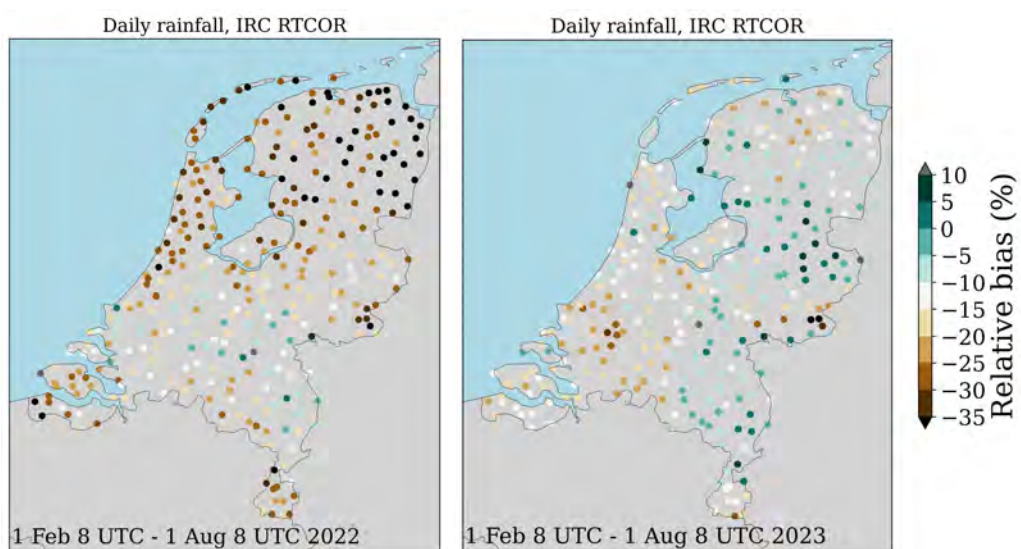


Figure 1.15: Spatial verification of radar daily precipitation accumulations from KNMI's real-time IRC product against daily accumulations from KNMI's manual rain gauge network over the period 1 February 8 UTC - 1 August 8 UTC for the year 2022 (left) and the year 2023 (right). Map made with Natural Earth. Free vector and raster map data ©natureearthdata.com.

- Develop regulation on the minimum distance of wind farms to weather radar sites. The current rise in the number of wind farms can lead to a substantial increase in the number of beam-blockage affected regions. Moreover, wind farms can result in persistent non-meteorological echoes that are difficult to remove. See Leijnse et al. (2022) for more information on the impact of wind farms on weather radars in Europe, including recommendations. Belmonte and Fabregas (2010) also show that wind turbines can lead to substantial blockage.

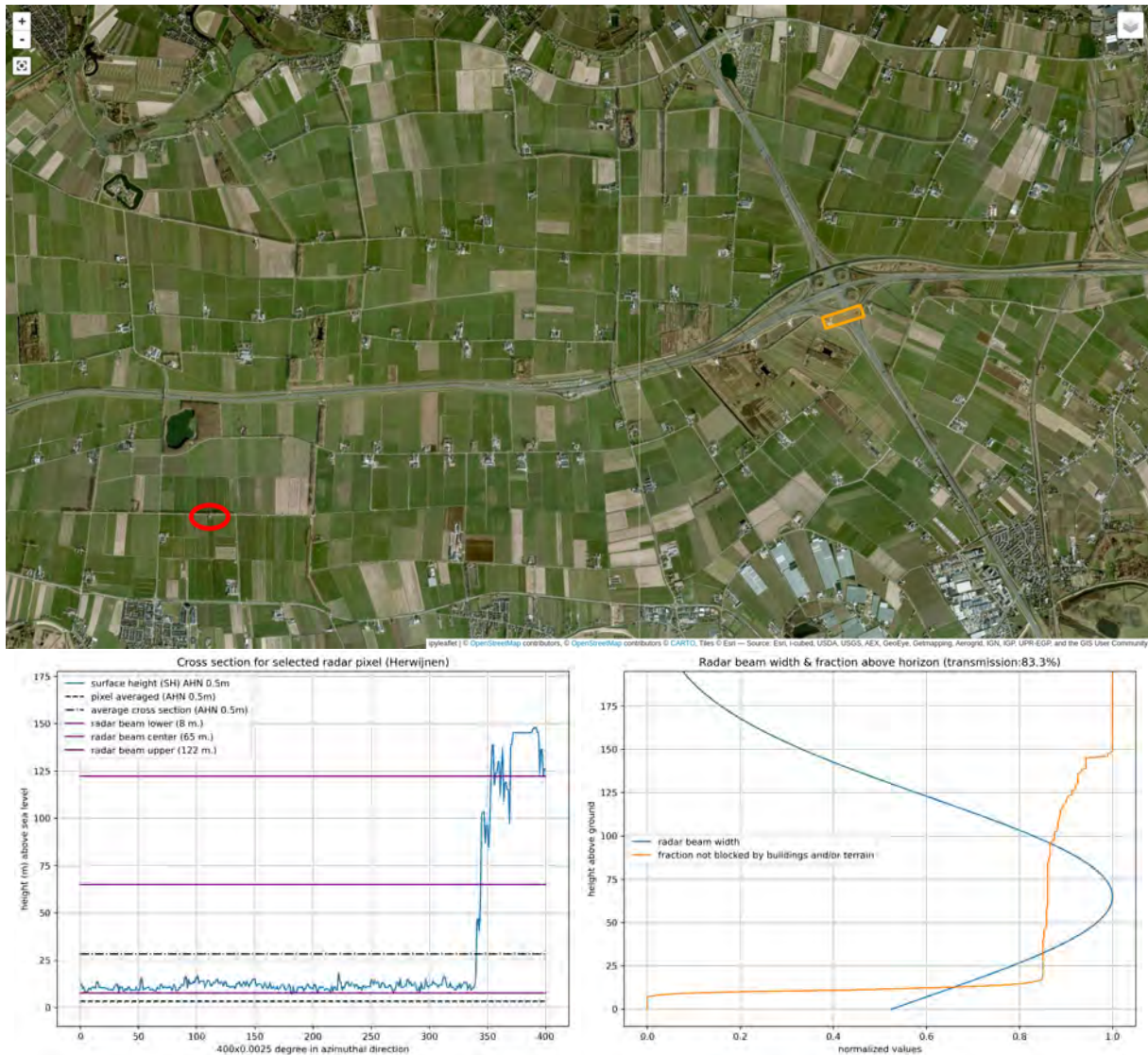


Figure 1.16: Effect of a wind turbine in easterly direction of the Herwijnen radar, near the Deil motorway junction, on beam blockage. The Herwijnen radar is located within the red oval. Based on AHN4. The transmission value is the part of the beam that is not blocked in this range bin.

1.4 Conclusions and recommendations

One method for beam-blockage computations was applied employing the open source library wradlib. Important insights have been gained on the effect of beam blockage on all operational dual-polarisation C-band radars relevant for the Belgian-Dutch-German border region and the KNMI radar Den Helder in the northwest of the Netherlands. The effectiveness of the beam-blockage correction was tested on 318 days of data from the KNMI radar in Herwijnen: it helps to partially correct for beam-blockage induced underestimation. Results from the KNMI IRC products show that beam-blockage in the northeast of the Netherlands has been reduced in the year 2023 compared to the year 2022. We expect that this is mainly the result of using the German radar in Borkum in 2023. In general, the Belgian-Dutch-German border region seems relatively well covered by radars, that observe from different directions and ranges, with generally only mild beam blockage for some regions. This study is probably relatively unique because it uses digital elevation model data with high spatial resolution, obtained from LiDAR, which is especially important in urban environments (Cremonini et al., 2016).

The following main recommendations are provided to further investigate beam blockage over the Netherlands and the Belgian-Dutch-German border region:

- Repeat the analyses for the Belgian and German radars employing similar digital elevation model data as the AHN data from the Netherlands, with much higher spatial resolution than the SRTM data. This is needed to provide a more accurate assessment of the beam blockage in the Belgian-Dutch-German border region. This could reveal that beam blockage is a larger issue than is assessed with the relatively coarse SRTM digital elevation model. We expect that the influence of nearby obstacles, such as buildings, is generally less of an issue for most Belgian and German radars in the Belgian-Dutch-German border region compared to the Dutch radars. Orography is expected to be the main cause of beam blockage, which will already be captured quite well with the SRTM data. Moreover, beam blockage due to nearby obstacles will be less severe for the German radar data given the higher lowest elevation scan angle of 0.5° . Also obtain 6-monthly or 1-year precipitation maps per radar for the Belgian and German radars to check whether beam blockage leads to underestimations. Ideally, also a spatial verification against rain gauge accumulations is performed. For Belgium, digital elevation model data are available as open data for Flanders¹⁰ and entire Belgium¹¹. For Germany, a portal gives an overview of digital elevation model data¹². Some lower spatial resolution data from this portal are freely available without cost, otherwise costs are involved. The dataset that seems most desirable for modelling radar beam blockage is only available for “Bundesbehörden”¹³. We advise to make these data open for future research studies on beam blockage;
- For the KNMI radar in Herwijnen, beam blockage can only be partly corrected for. Normal propagation conditions were assumed. We advise to study the occurrence of propagation conditions in time. Are normal propagation conditions common or are radar beams often refracted more towards or away from the Earth’s surface, implying that a larger or smaller part of the radar beam is blocked? Refraction depends on temperature and moisture gradients in the atmosphere. Vertical refractivity gradients could be computed from radiosonde or numerical weather prediction model output (Bech et al., 2003, 2007; Steiner and Smith, 2002). We recommend to explore whether refractivity gradients, the associated radar beam propagation and needed beam-blockage correction could be computed in a real-time fashion. Very close to radar sites, also radar data could be employed for computing the refractive index using fixed ground targets (Fabry et al., 1997);

¹⁰<https://overheid.vlaanderen.be/en/producten-diensten/digital-elevation-model>

¹¹<https://publish.geo.be/geonetwork/srv/api/records/af70738f-e738-11ec-be46-186571a04de2>

¹²https://gdz.bkg.bund.de/index.php/default/digitale-geodaten/digitale-gelandemodelle.html?__store=default

¹³<https://gdz.bkg.bund.de/index.php/default/digitale-geodaten/digitale-gelandemodelle/digitales-oberfaechenmodell-dom1.html>

- Rerun the analyses every few years for the Dutch radars once a new version of the Dutch DSM becomes available. This also holds for the Belgian and German radars once their DSM data are used;
- The dual-polarisation variable specific differential phase K_{dp} is immune to partial beam blockage in the sense that it is a phase measurement and not a power measurement. The part of the measurement volume that is blocked, will still not be sampled, though. First, a method employing the so-called self-consistency relationship of K_{dp} and horizontally polarised radar reflectivity factor (Z) (and differential reflectivity) could be explored to correct for beam blockage (Lang et al., 2009; Zhang et al., 2013). Second, K_{dp} could be used directly to estimate rainfall intensity. This can only be reliably applied in case of liquid precipitation and moderate to heavy rainfall as indicated by the value of the radar reflectivity factor (which may already be reduced too much because of beam blockage). These conditions will not always be met, especially for the most beam-blockage affected areas, which are typically at longer range from a radar, where the radar beam may only experience solid precipitation;
- The analyses for the Den Helder radar site, where nearby buildings and other obstacles are abundant, shows that the use of beam-blockage detection via digital elevation model data is not always straightforward. A careful and detailed analysis should be carried out, preferably by extending the local analysis with the KNMI tool to identify obstacles causing beam blockage. Especially for the Den Helder radar, many obstacles are present that could be analysed. This can help to take action, such as cutting trees. For instance, the group of trees northeast of the Herwijnen radar pose a literally growing problem. The tool should also be expanded with DSM data from Belgium and Germany to identify obstacles near the Belgian and German radar sites. Finally, the beam-blockage analyses itself should be repeated for simulated range bins with different radial resolutions (much shorter than 5 m). Especially, because the wradlib algorithm only uses the digital elevation model data from the middle of a range bin;
- Jointly investigate beam blockage and possible legislation on radar site protection (wind farms, radio interference) with owners of radars: the national meteorological services in Belgium (RMI), Germany (DWD) and the Netherlands (KNMI), and VMM;
- Apply beam blockage correction to the data from the radars in Houthalen-Helchteren and Wideumont and evaluate the performance of precipitation estimates over a 1-year period.

Some remaining recommendations are:

- Another method for beam-blockage detection and correction searches for azimuthally bounded areas of underestimation that are radially consistent. This only uses long-term radar precipitation accumulations and has been tested on 36-month accumulations for radars in the western continental United States of America (McRoberts and Nielsen-Gammon, 2017). A similar approach has been applied by Overeem et al. (2009) by comparing annual rainfall accumulations to those from adjacent azimuth sectors. In case of a strong decrease in annual rainfall, a range bin value is replaced by an interpolated value from the nearest nonblocked azimuth sectors. These kind of methods could also be applied to data from radars covering the Belgian-Dutch-German border region. Results could be contrasted to those based on digital elevation model data and K_{dp} ;
- For some Belgian or German radars, also higher elevation scans may be affected by orography. Hence, the beam-blockage analyses could be extended to those scans.

Chapter 2

Automatic correction for the electronic calibration of the radar

2.1 Introduction to hardware calibration monitoring with the sun

Quantitative precipitation estimation with radars starts with signal processing at the radar site. This typically includes Doppler clutter filtering to remove the effect of stationary non-meteorological echoes on the received power. Essential is the conversion from echo powers to radar reflectivity factors. It is important to detect and correct hardware-related errors, because these can have a large impact on the quality of precipitation estimates. This requires monitoring and calibration in the signal processor (Frech et al., 2017). Calibration concerns the hardware of the radar and not the adjustment with rain gauge data. Here, two specific hardware calibration issues are addressed:

- Offsets in radar antenna pointing accuracy, i.e., azimuth & elevation offsets. These can lead to deviations in the location of estimated precipitation with respect to the true location of the radar sampling volume, especially at far range from a radar;
- The sensitivity of the radar receiver, i.e., offsets in the measurement of received power. Degradation of components can result in receiver offsets. As far as is possible, the receiver channel is calibrated once a year for the KNMI radars. Moreover, an electric signal is injected to check the signal booster every 5 minutes. Offsets can result in under- or overestimation of precipitation.

These offsets can be determined by solar monitoring. An example of a solar interference (artifact) is visible as a spoke in easterly direction for the KNMI radar in Den Helder (Figure 2.1). Typically, uncorrected radar reflectivity factor data are employed for solar monitoring. The corrected radar reflectivity factors have undergone Doppler clutter filtering, which can attenuate the solar interference (Huuskonen et al., 2014). In this case, the solar interference is also clearly visible for the corrected reflectivity. Because the sun is a constant source of radiation, it is visible over (almost) the entire ray of this scan (74.9 km range) for the 94.5° and 95.5° azimuth sectors. Note that each scan has its own maximum range. Since the position of the sun is exactly known, the radar antenna pointing accuracy can be verified. In this example, the azimuth of the sun is 94.70°. Indeed, the strongest reflectivity is observed for the ray with azimuth 94.5°. The elevation angle of the sun is 19.82°, which is very close to the 20° elevation scan angle. In addition, the received solar flux is computed from the received solar power employing the uncorrected reflectivity data. Finally, this received solar flux can be compared to the solar flux observed by a monitoring station in Canada. The higher the received solar flux, the better the overlap between the $\sim 0.5^\circ$ ¹ solar beam and the $\sim 1^\circ$ radar beam. In case only the lower part of the radar beam intersects

¹Due to the varying Earth-sun distance it varies from 0.524° in July to 0.542° in January.

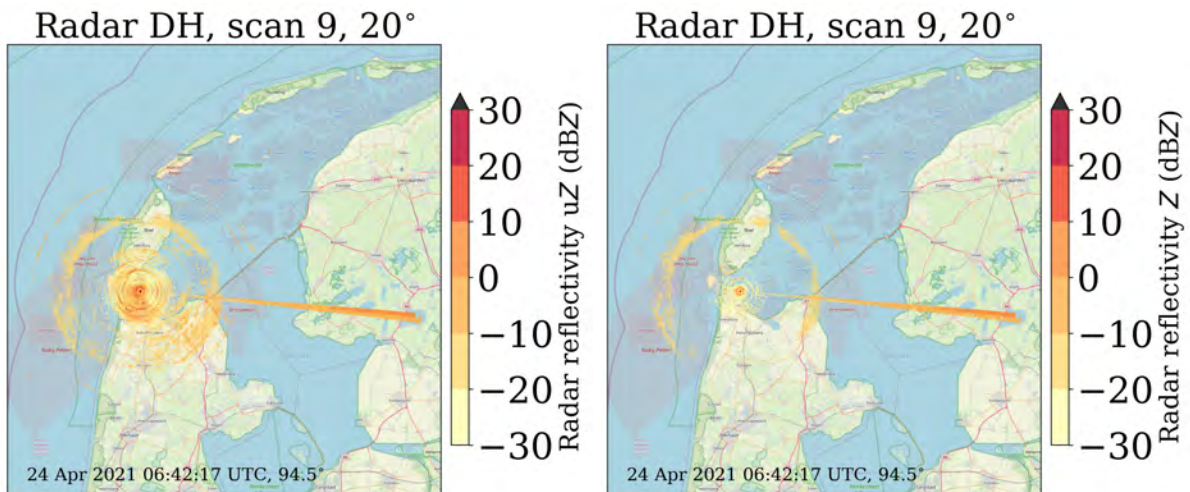


Figure 2.1: Illustration of a solar interference in polar radar data. Map of a domain around the KNMI radar in Den Helder, the Netherlands, with the uncorrected (left) and corrected (right) horizontally polarised radar reflectivity factor (dBZ) for the 20° elevation scan. Map data ©OpenStreetMap contributors 2023. Distributed under the Open Data Commons Open Database License (ODbL) v1.0.

with the upper part of the sun beam, the overlap is much smaller and the received power will hence be much lower. Note that solar monitoring does not require a sunny day, because solar radiation at C-band propagates through clouds.

Here, the solar flux is 19.70 dB and 14.32 dB for the 94.5° and 95.5° azimuth sectors, respectively. The observed solar flux is 21.30 dB after conversion from S-band to C-band, the typical microwave frequency band employed by weather radars in the Belgian-Dutch-German border region. Because this conversion is an approximation, the received solar flux by a weather radar can be typically 1–2 dB lower. Also the increase in sunbursts at S-band does not need to be the same as that at C-band. The offset is -1.6 dB for the 94.5° azimuth, which is well aligned (-0.2° azimuth offset and 0.18° elevation offset). Since the 95.5° azimuth is less well aligned with the actual sun position, the received solar flux is 7 dB off. This already points to a limitation of solar monitoring in case solar interference is found in multiple azimuth sectors. More information on radar hardware monitoring using the sun and the underlying physics is, for instance, provided by Holleman and Beekhuis (2004); Huuskonen and Holleman (2007). This chapter focuses on analyses for the Den Helder and Herwijnen radar in the Netherlands, for which KNMI has developed custom tools. Other radars relevant for the Belgian-Dutch-German border region are not considered.

2.2 Datasets & Methodology

2.2.1 Radar data

KNMI operates two C-band dual-polarisation weather radars in the Netherlands. One is located in the northwest in Den Helder, and one in the centre in Herwijnen (Figure 1.1). Technical details on the KNMI radars are provided by Beekhuis and Mathijssen (2018). The radars perform 16 azimuthal scans of 360° around a vertical axis every 5 minutes. The elevation scan angles are 0.3°, 0.8°, 1.2°, 2.0°, 2.8°, 4.5°, 6.0°, 8.0°, 10.0°, 12.0°, 15.0°, 20.0°, 25.0°, and 90.0°. The last one is not considered in this study given the maximum possible sun elevation angle. The lowest elevation scan angle of 0.3° is used for three different elevation scans (or sweeps), whereas the other elevation angles are only used in one scan. The analyses focus on the period between the radar maintenance in spring 2021 and the radar maintenance

in autumn 2021. It is assumed that changes in antenna pointing and receiver sensitivity mainly occur during maintenance. Moreover, this period covers the extreme rainfall event mid-July 2021 and allows for collecting more observations. Taking into account the dates of maintenance, data from the following periods were obtained: 23 April – 24 November 2021 (Den Helder; 99.7% availability) and 15 April – 27 October 2021 (Herwijnen; 96.0% availability; the lower availability is mainly caused by radome maintenance). For the Den Helder radar, also analyses based on data from the 30 days preceding this period are presented to investigate possible changes in offsets due to maintenance.

2.2.2 Solar flux monitoring station data

The daily recorded solar flux at S-band, $F_{10.7}$, is obtained from the Dominion Radio Astrophysical Observatory (DRAO²) in Canada³ in the framework of the Solar Radio Monitoring Program serviced by the National Research Council and Natural Resources Canada, with support from the Canadian Space Agency. Using this data, the solar flux at C-band (dB) is estimated (Holleman and Beekhuis, 2004):

$$F_C = \frac{\log_{10}(0.71 \times (F_{10.7} - 64) + 126)}{\log_{10}(10)}. \quad (2.1)$$

2.2.3 Algorithm

A solar monitoring tool, which has been developed at KNMI, is employed for radar hardware monitoring. A two-stage method is applied to compute the sun hit power. In the first stage, only range bins above an 8-km height are employed, in order to avoid precipitation echoes. In case less than 20 km of the ray for a chosen elevation scan angle is above 8 km, the last 20 km of this ray is selected, irrespective of its height. For instance, the lowest elevation scan does not even reach the 8-km height, but its highest ~ 50 range bins are employed for the analyses. For each 1° azimuth sector, the received solar power (dBm) is computed from the uncorrected radar reflectivity factor (uZ) for a range bin in case uZ is not equal to the “no data” (or “missing data”) value (SIGMET, 1998; Holleman and Beekhuis, 2004; Huuskonen and Holleman, 2007):

$$P_{\text{solar}} = uZ - 20 \log_{10} r + a_{\text{gas}} \times r + C, \quad (2.2)$$

with r the range to the radar (km) for the considered range bin, a_{gas} the two-way gaseous attenuation (0.016 dB km^{-1}) that represents atmospheric attenuation between radar and target. The radar constant C (dB) depends on properties of the radar, such as the wavelength, and includes losses such as waveguide, receiver and radome losses. This equation takes into account the range correction ($1/r^2$). The received solar radiation is a weak, but constant source of radio frequency radiation over the entire ray. The $1/r^2$ inverse-square law introduces a range dependency of the solar interference that results in increased values for uZ . This is resolved in the equation above (Holleman and Beekhuis, 2004; Huuskonen and Holleman, 2007). The received solar power is computed for each range bin. Subsequently, for a chosen azimuth the received solar powers are averaged over all range bins with valid data. When the fraction of range bins with valid data is smaller than 0.7, no computations are provided for the chosen azimuth and the program proceeds to the next azimuth. Otherwise, the second stage computations start.

In the second stage, the above recipe is repeated, but now only range bins above a 4-km height are used. In addition, an extra selection criterion is employed that stops the analysis for a chosen range bin when the computed received solar power for that range bin deviates more than 2 dB from the averaged received solar power computed in the first stage. Next, from the averaged received solar power over

²<https://www.spaceweather.gc.ca/forecast-prevision/solar-solaire/solarflux/sx-en.php>

³ftp://ftp.seismo.nrcan.gc.ca/spaceweather/solar_flux/daily_flux_values/fluxtable.txt

all range bins $10 \times \log_{10}(1.2/\tau)$ is subtracted, with τ the pulse duration, and 1.2 a factor between bandwidth and $1/\tau$.

Finally, the averaged received solar power is corrected to obtain the received solar flux (dB) for the chosen azimuth:

$$P_{\text{solar}}^{\text{corrected}} = 130 + P_{\text{solar}} + A_{\text{Rx}} 10 \times \log_{10}(\text{AntArea}) + A_{\text{avgattn}} + A_{\text{onepol}}, \quad (2.3)$$

with A_{Rx} the losses between reference and feed (2.57 dB for Herwijnen and 2.36 dB for Den Helder; Rx stands for received signals), AntArea the effective area of the antenna (9.440 m² for Herwijnen and 10.819 m² for Den Helder), A_{avgattn} the averaging and overlap losses for 1° (dB), and A_{onepol} losses due to one-pol Rx (3.01 dB). Note that the presented algorithm largely follows (Holleman and Beekhuis, 2004), but that they use a one-stage method where only range bins beyond 200 km are considered.

The solar elevation and azimuth are computed from the geographical position, date and time, employing the equations and constants from the WMO Guide to Meteorological Instruments and Methods of Observations (CIMO, WMO no. 8), annex 7.D (equations have been slightly modified and extended, though). These computations are performed for each 1° azimuth sector that successfully passed the two-stage method, where the time is computed from the start time and antenna velocity of the scan. This is repeated for all elevation scans. Data are only kept when the elevation and azimuth angle of the scan differ at most five degrees from the corresponding sun elevation and azimuth angle.

The following algorithms or settings are evaluated:

- Default algorithm as described above with a fraction of range bins with valid data (i.e., higher than the missing or nodata value of $Z = 0 \text{ mm}^6 \text{ m}^{-3}$) of at least 0.7;
- In case of a true solar hit, you expect that almost all range bins are affected. To remove more incorrectly classified solar hits, the algorithm is also run with a fraction of range bins with valid data of at least 0.9. This may help to remove hits due to radio interference, which can only cover part of a ray;
- In this study, an extended version of the algorithm has been developed, called strict filtering. Rays from adjacent azimuth sectors are also taken into account to remove hits caused by radio interference or precipitation, that can cover multiple rays (Figures 2.4 and 2.5). The two adjacent rays are selected that are 2° from the considered ray. E.g., select rays for azimuth sectors 10° & 14°, when ray with azimuth sector 12° is considered. If one or two of the adjacent rays has a fraction of range bins with valid data larger than 0.1, the considered ray is not selected. Note that this approach could also discard some true solar hits. This algorithm is tested with a fraction of range bins with valid data of at least 0.9.

A second program is used to estimate the azimuth and elevation biases on a daily basis or over the entire 6-month periods based on the output provided by the algorithms described above. This assumes a Gaussian shape for the combination of the received solar power by the antenna, the antenna beam shape and the azimuthal beam averaging (Huuskonen and Holleman, 2007).

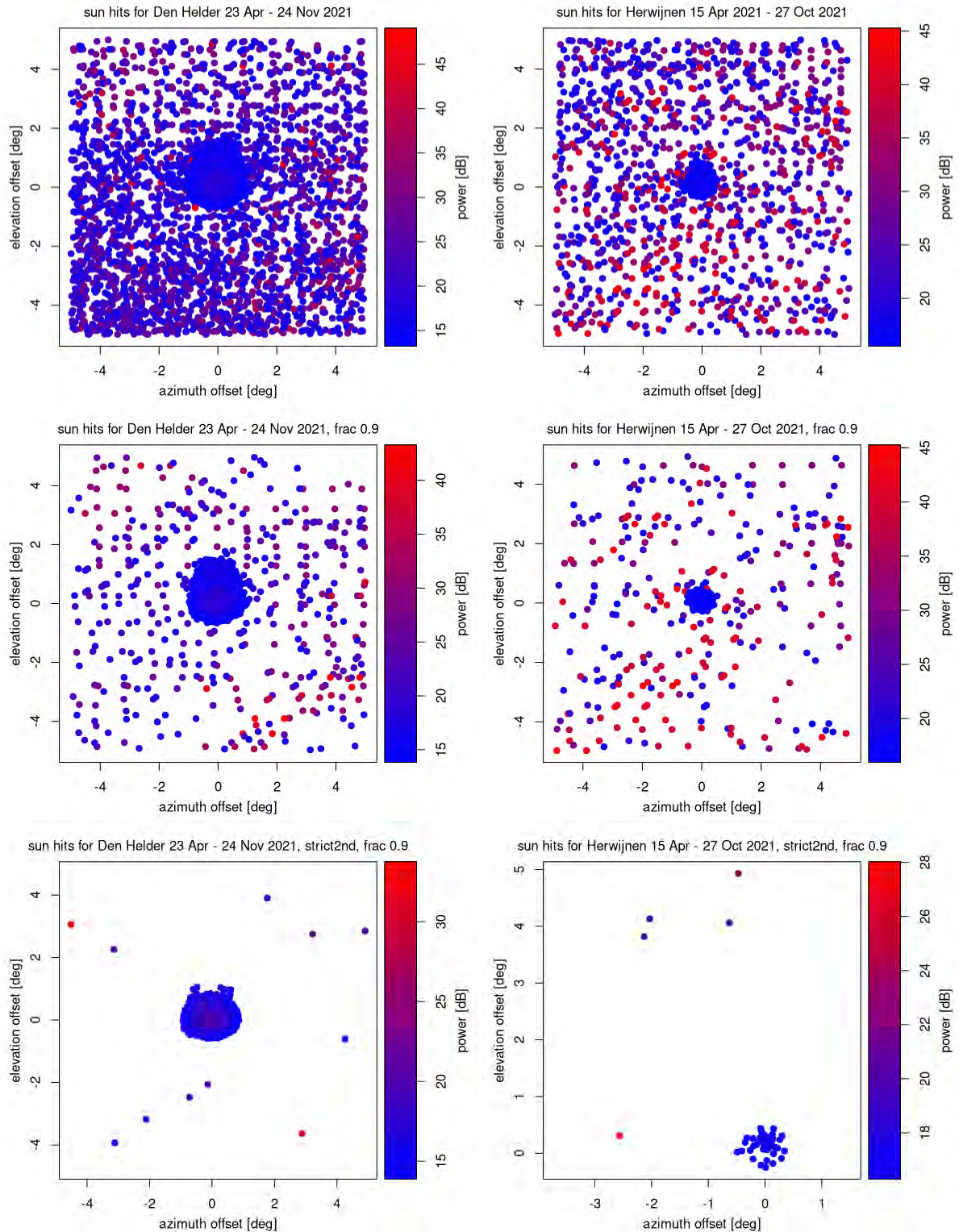
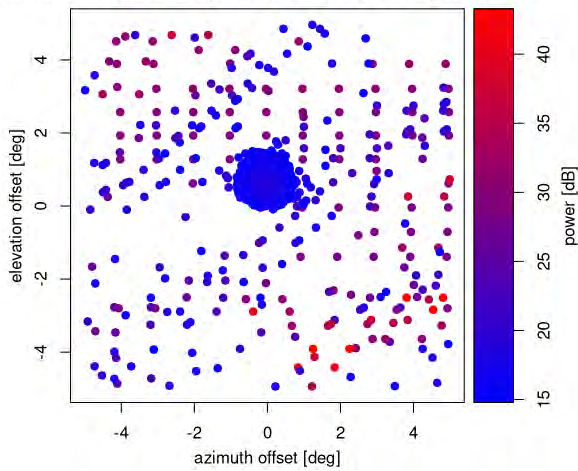
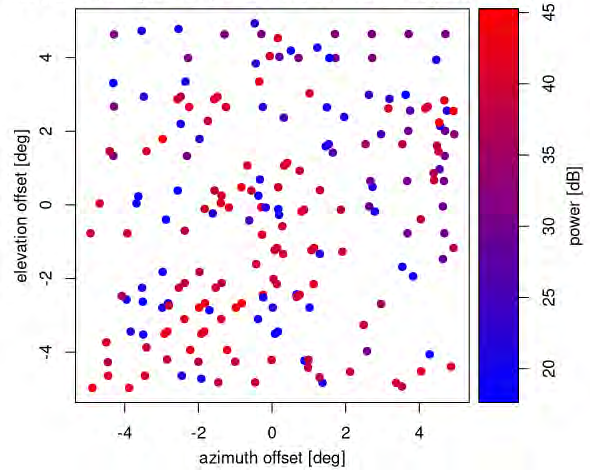


Figure 2.2: Elevation versus azimuth offset over the ~ 6 -month periods for the Den Helder (left) and Herwijnen (right) radars. Note that the scale of horizontal and vertical axes is not the same for all graphs. The first row shows the results for the default algorithm. The second and third row show the results for the algorithm with a fraction of range bins with valid data of 0.9. Moreover, for the third row also the strict filtering has been applied.

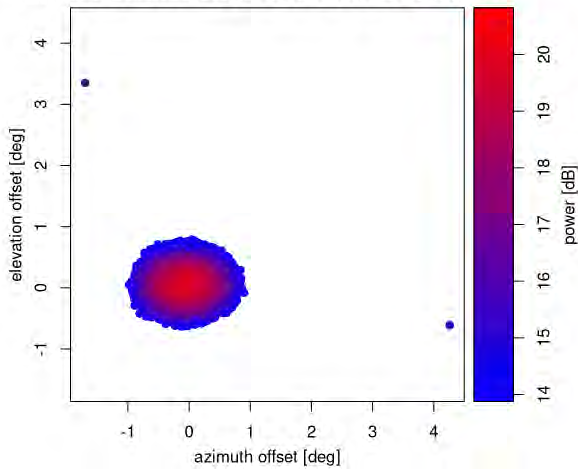
sun hits for Den Helder 23 Apr - 24 Nov 2021, scan 0.3 degrees, frac 0.9



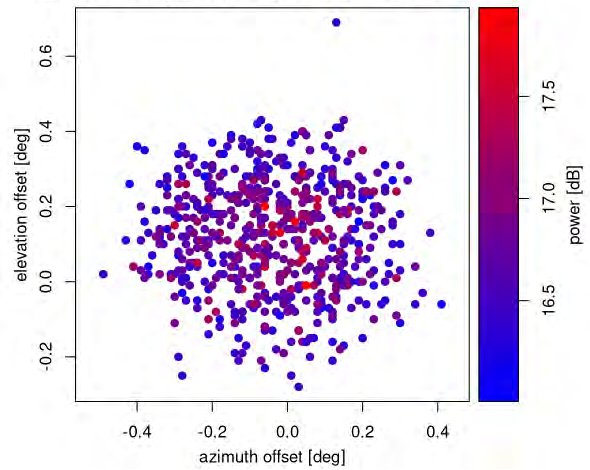
sun hits for Herwijnen 15 Apr - 27 Oct 2021, scan 0.3 degrees, frac 0.9



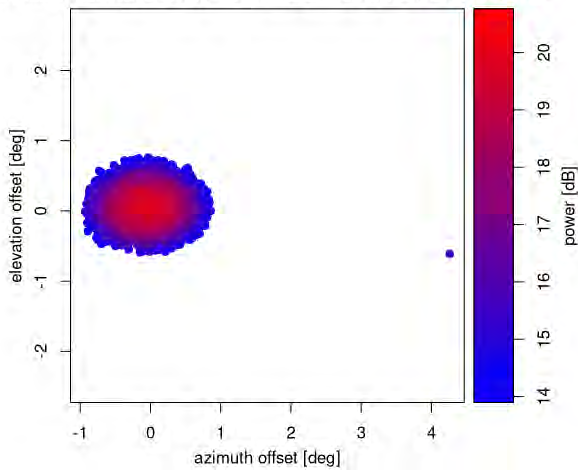
sun hits for Den Helder 23 Apr - 24 Nov 2021, frac 0.9, highest el.



sun hits for Herwijnen 15 Apr - 27 Oct 2021, frac 0.9, highest el.



sun hits for Den Helder 23 Apr - 24 Nov 2021, frac 0.9, strict2nd, highest el.



sun hits for Herwijnen 15 Apr - 27 Oct 2021, frac 0.9, strict2nd, highest el.

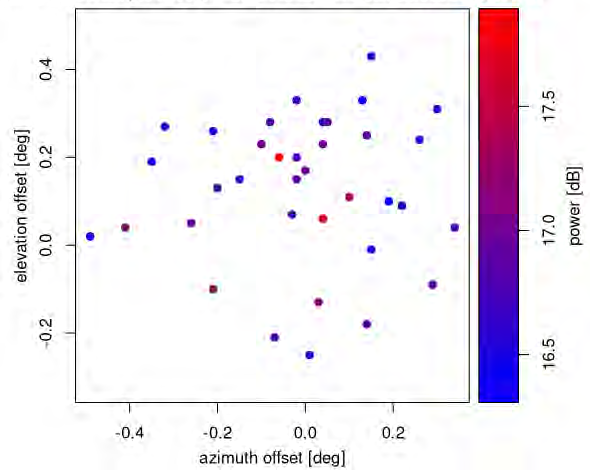


Figure 2.3: Elevation versus azimuth offset for the lowest elevation scans (top panel) and the five highest elevation scans without (middle panel) and with (bottom panel) strict filtering. For the ~6-month periods for the Den Helder (left) and Herwijnen (right) radars. Note that the scale of horizontal and vertical axes is not the same for all graphs.

2.3 Results

2.3.1 Elevation and azimuth offsets

Elevation versus azimuth offsets of all hits in the ~ 6 -month period are visualised for the Den Helder and Herwijnen radar separately (Figure 2.2). For the default algorithm, a dense, circular point cloud is found. Many hits are located outside this point cloud (outliers, although these can still be solar hits), having considerable negative or positive offsets up to 5° . Compared to the Den Helder radar, the point cloud is smaller, which is likely associated with the much lower number of hits for the Herwijnen radar. Raising the value for the fraction to 0.9 removes a large part of these outliers. Strict filtering further decreases the number of outliers, to just 5 for the Herwijnen radar and just 11 for the Den Helder radar, but still some large outliers are present.

Next, the performance for the lowest elevation scan angle (0.3°) and the five highest elevation scan angles (10.0° , 12.0° , 15.0° , 20.0° , 25.0°) are compared (Figure 2.3). The scatter and number of outliers are much larger for the lowest elevation scan data (top panel) compared to the data from the five highest elevation scans (middle panel). A reason for this is severe refraction of the sun beam at low elevation angles and the higher probability of encountering precipitation along a large part of the ray (although here a minimum height of 4 km is used, thus avoiding precipitation). Because of this, Huuskonen et al. (2014) even discard data from elevation scan angles below 1° . It is hypothesized that the use of data from only ~ 50 range bins for the lowest elevation scan in the first stage of the algorithm, may increase the vulnerability to artifacts not related to the sun and hence may contribute to the scatter in Figure 2.3.

Only two strong outliers are present for the Den Helder radar for the five highest elevation scans. The middle of the point cloud shows the highest powers. The dimensions of the point cloud are much smaller for the Herwijnen radar. Applying strict filtering (bottom panel) removes one severe outlier for the Den Helder radar and leads to a large reduction in the number of hits for the Herwijnen radar. When this strict filtering is applied to the data from the lowest elevation scans (not shown), very few points are left for the Den Helder radar, whereas still large outliers are present, and no points are left for the Herwijnen radar.

Table 2.1 shows that the average elevation bias (0.014 – 0.060°) and azimuth bias (-0.028 – 0.047°) are small, but based on very few data points for the Herwijnen radar in case strict filtering is applied. The 11 remaining outliers for the Den Helder radar after strict filtering, may negatively affect the accuracy of the estimated biases. Applying the strict filtering to the data from the five highest elevation scans results in similar biases for the Den Helder radar. Differences for the Herwijnen radar are sometimes larger, but note that the analyses are based on few data points. The point cloud for the five highest elevation scans is rather wide for the Den Helder radar, $\sim 2^\circ$ in azimuth and $\sim 1.5^\circ$ in elevation (Figure 2.3).

An example of an erroneously classified solar hit, caused by radio interference, is shown in Figure 2.4 (top panel, right). This is the outlier in the upper left corner of the elevation offset versus azimuth offset figure (top panel, right). Applying strict filtering removes this outlier, but also leads to a substantial thinning out of the point cloud (bottom panel).

Large-scale precipitation can also result in erroneous solar hits. The entire ray can be filled with precipitation near the position of the sun. For the event in Figure 2.5, this leads to five consecutive azimuth sectors wrongly identified as a solar hit (297.5° – 301.5°) for one of the 0.3° elevation scans. The accompanying received solar flux ranges from 27.63–28.72 dB, much higher than the observed solar flux of ~ 21.2 dB. Also selection of a higher fraction of 0.9 instead of 0.7 does not remove these, but the strict filtering successfully removes these.

An azimuth bias α results in a lateral displacement of the precipitation as noted by a radar. The lateral

Table 2.1: Offsets based on solar monitoring averaged over the ~ 6 -month period for the KNMI radars in Den Helder and Herwijnen.

Radar	Number of points	Elevation bias ($^{\circ}$)	Azimuth bias ($^{\circ}$)	Received solar flux (dB)	DRAO observed solar flux (dB)
<i>Strict filtering & fraction of 0.9:</i>					
Den Helder	896	0.020	-0.045	19.36	21.42
Herwijnen	40	0.034	-0.046	17.39	21.40
<i>Only five highest elevations & fraction of 0.9:</i>					
Den Helder	2184	0.014	-0.047	19.60	21.42
Herwijnen	580	0.060	-0.028	17.18	21.40
<i>Only five highest elevations & strict filtering & fraction of 0.9:</i>					
Den Helder	1232	0.013	-0.042	19.77	21.42
Herwijnen	36	0.005	-0.046	17.32	21.40

displacement d (km) can be computed for a given range r (km) from the radar:

$$d = r \times \tan \alpha \quad (2.4)$$

The highest azimuth bias offset based on data from all elevations in table 2.1 is 0.046° and found for the Herwijnen radar. This would result in a lateral displacement of ~ 0.10 km in the south of the Dutch province of Limburg (125 km range) and a lateral displacement of ~ 0.16 km at 200 km range. These are small displacements and can be considered negligible given representativeness errors of radar precipitation estimates for observing precipitation at the Earth's surface.

2.3.2 Receiver offsets

The azimuth (angular) and elevation biases and the received and observed solar fluxes are now calculated per day and are visualised in Figure 2.6 for 30-day periods. The antenna pointing offsets are small for the Den Helder radar, except for an outlier that may be related to the relatively low number of solar hits. For the Herwijnen radar, the elevation biases are larger and the azimuth biases are small, except that both have one outlier. The solar flux is generally within ~ 1 – 2 dB from the observed flux for the Den Helder radar, with somewhat better agreement compared to the period preceding the maintenance in spring (top left panel). For the latter, the azimuth biases are smaller, though. To conclude, the effect of maintenance for the Den Helder radar seems small. The number of solar hits for the Herwijnen radar is much lower than for the Den Helder radar, and is too low to draw firm conclusions. Hence, the ~ 3 – 4 dB underestimation of the solar flux is only an indication for an underestimation of the received solar flux. These analyses have been run for the fraction of 0.7. This implies that a lot of outliers are present (Figure 2.2), that may limit the validity of the results. Note that applying a higher fraction of 0.9 or strict filtering would lead to a severe reduction in the number of data points, that could also lead to deviations.

2.3.3 Discussion

- Most analyses are based on the entire ~ 6 -month period. This assumes that offsets only change during maintenance, but not during a period;
- Systematic offsets are assumed to be the same for different elevation scans. The highest elevation scans, that are least important for precipitation estimation, provide the most precise offset

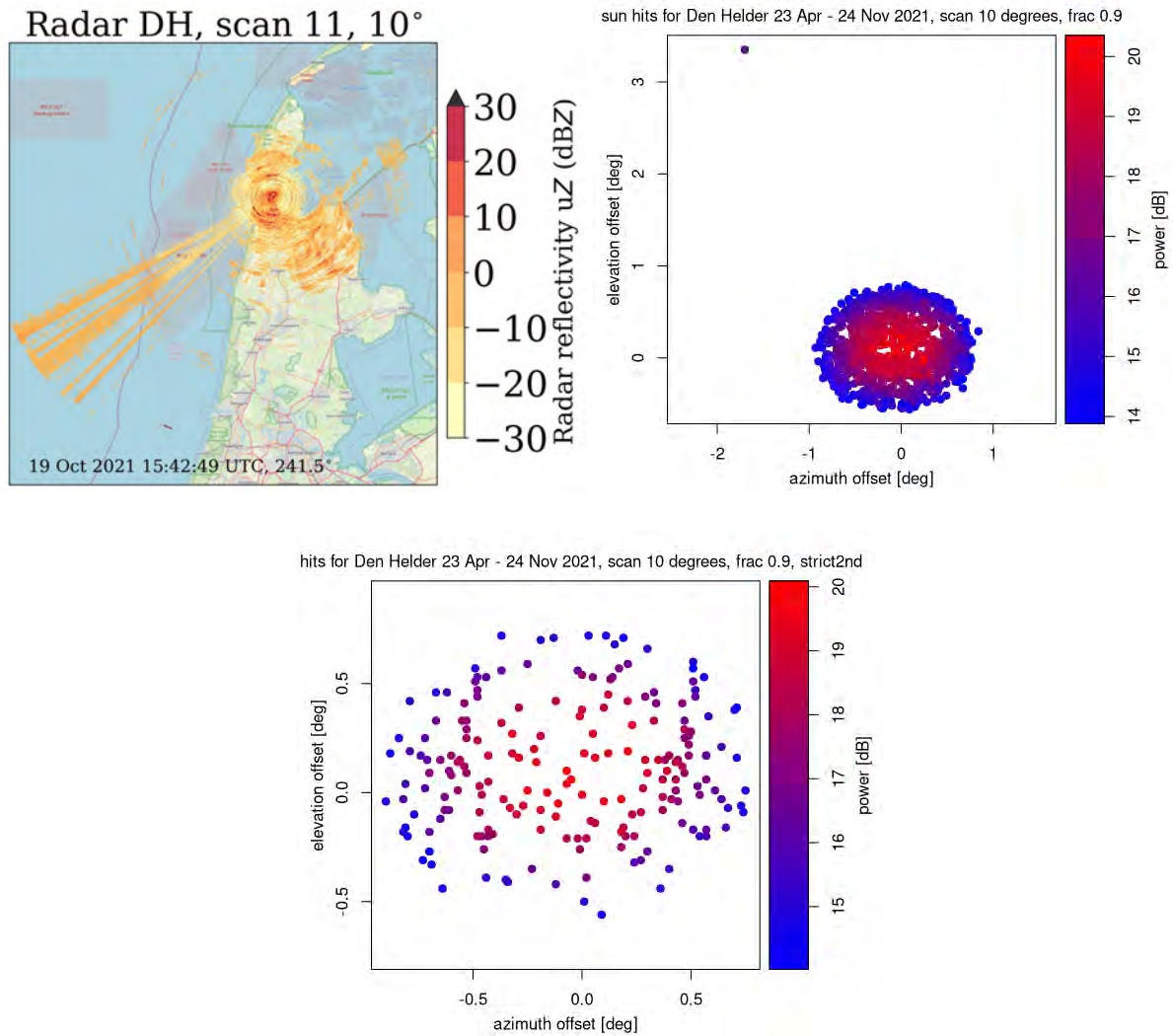


Figure 2.4: Illustration of radio interference in polar radar data. Map of a domain around the KNMI radar in Den Helder, the Netherlands, with the uncorrected horizontally polarised radar reflectivity factor (dBZ) for the 10° elevation scan (top panel, left). The corresponding elevation versus azimuth offset before (top panel, right) and after applying strict filtering (bottom panel). Map data ©OpenStreetMap contributors 2023. Distributed under the Open Data Commons Open Database License (ODbL) v1.0.

data, and are assumed to be representative for the lower elevation scan offsets, that are the most relevant for precipitation estimation, but contain a lot of outliers;

- In the computation of the received solar power, receiver losses are taken into account and assumed to be constant. Their values have been determined during the site acceptance test of the radar;
- Using a higher fraction of 0.9 instead of 0.7 and the developed strict filtering method helps to substantially reduce the number of outliers, but also results in much fewer data points left. Although the daily time series in Figure 2.6 for the Den Helder radar seem trustworthy, Figure 2.2 shows that many outliers are present for a fraction of 0.7. The time series could be obtained using a higher fraction or the strict filtering method. However, this will result in a large reduction in the number of solar hits, which could result in less days for which offsets can be computed. Note that the average offsets over the ~6-month period with additional selections are already provided in Table 2.1, confirming the small elevation, azimuth, and receiver biases;

Radar DH, scan 15, 0.3°

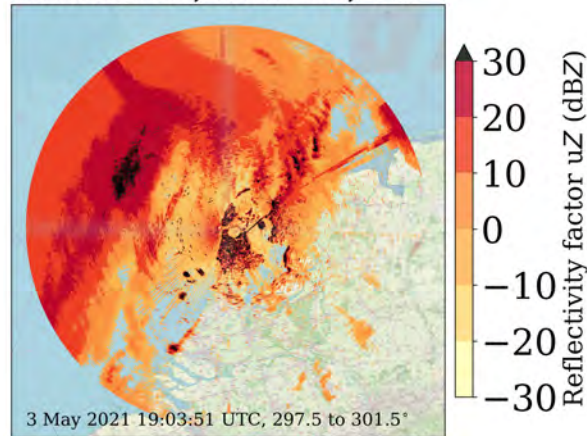



Figure 2.5: Illustration of precipitation in polar radar data for the 0.3° elevation scan. Map data ©OpenStreetMap contributors 2023. Distributed under the Open Data Commons Open Database License (ODbL) v1.0.

2.4 Conclusions and recommendations

We assessed antenna pointing accuracy and receiver sensitivity for the two KNMI radars in the Netherlands based on a ~ 6 -month period that includes the extreme rainfall from mid-July 2021 in the Belgian-Dutch-German border region. Azimuth and elevation biases are shown to be small, resulting in only small lateral displacement of the precipitation locations. The receiver offsets for the Den Helder radar are within the expected ~ 1 -2 dB bandwidth, but those for the Herwijnen radar are too large (~ 3 -4 dB), which would result in underestimation of precipitation. An important disclaimer is that the analyses for the Herwijnen radar are based on few data, and hence results are not conclusive. The reason for the low number of hits for the Herwijnen radar should be investigated. A hypothesis is that the received solar radiation is often below the receiver's sensitivity.

We provide the following additional recommendations:

- In case of moderate or heavy rainfall, the dual-polarisation variable specific differential phase (K_{dp}) can be employed for rainfall estimation, which is immune to hardware calibration errors (see Figure 3.6 in Chapter 3);
- For the beam-blockage analyses, normal propagation conditions are assumed. Strong temperature and moisture gradients can refract the radar signals, resulting in computed offsets in azimuth or elevation of the antenna and a weaker or stronger received signal from the sun. Vertical refractivity gradients could be computed from radiosonde or numerical weather prediction model output (Bech et al., 2003, 2007). We recommend to explore whether refractivity gradients and the associated radar beam propagation could be computed, and only select solar hits in case of normal propagation conditions;
- The solar hit data are analysed per day. Sometimes, days are missing due to too few data points or due to outliers that escape current filtering efforts, which prevents a reliable computation of offsets. This can, for instance, be caused by precipitation that is persistent during daylight conditions on a particular day.
- A possible way to further exclude outliers as much as possible, is to only select solar hits when the elevation and azimuth angle of the scan differ at most two instead of five degrees from the corresponding sun elevation and azimuth angle. The chosen limits are a bit arbitrary and this



assumes that deviations are indeed within these limits. Partly overlapping solar hits would be removed by this approach. The question is whether we need these weaker solar hits. In addition, range bins for which the received solar power deviates more than, e.g., 4 dB from the observed DRAO solar power could be discarded, which could also remove hits from the point cloud.

- Follow the position of the sun with a radar antenna during a dry day and perform a detailed investigation. This will result in many solar hits and enhance the probability of an accurate assessment of elevation, azimuth and receiver offsets. This strategy can result in a high amount of good quality data in a short period of time, but is difficult to arrange due to the operational nature of the radars;
- The tool for solar monitoring should be further explored and different parameter settings should be tested. The tool should be made operational to allow for continuous monitoring. In addition, it could be explored whether receiver offsets could be automatically corrected for. For instance, by increasing the radar reflectivity factor in case of larger than -2 dB offsets. This automatic correction for the electronic calibration of the radar should be further explored and should also incorporate the variable differential reflectivity. Automatic monitoring including signalling would already allow for taking actions regarding maintenance;
- Investigate which algorithms are employed for solar monitoring in the framework of the European Meteorological Network (EUMETNET) Operational Program on the Exchange of Weather Radar Information (OPERA) (Holleman et al., 2022). They use the solar monitoring as implemented in Baltrad. This is based on the programs used for the analyses in this chapter, although differences in code and settings may occur. The solar monitoring results from OPERA reveal a similar receiver offset for the Herwijnen radar as found in this study (not shown);
- The solar monitoring from OPERA or possible solar monitoring by RMI, VMM or DWD, may be used to investigate the offsets for all (other) C-band radars in the Belgian-Dutch-German border region around the July 2021 casestudy.

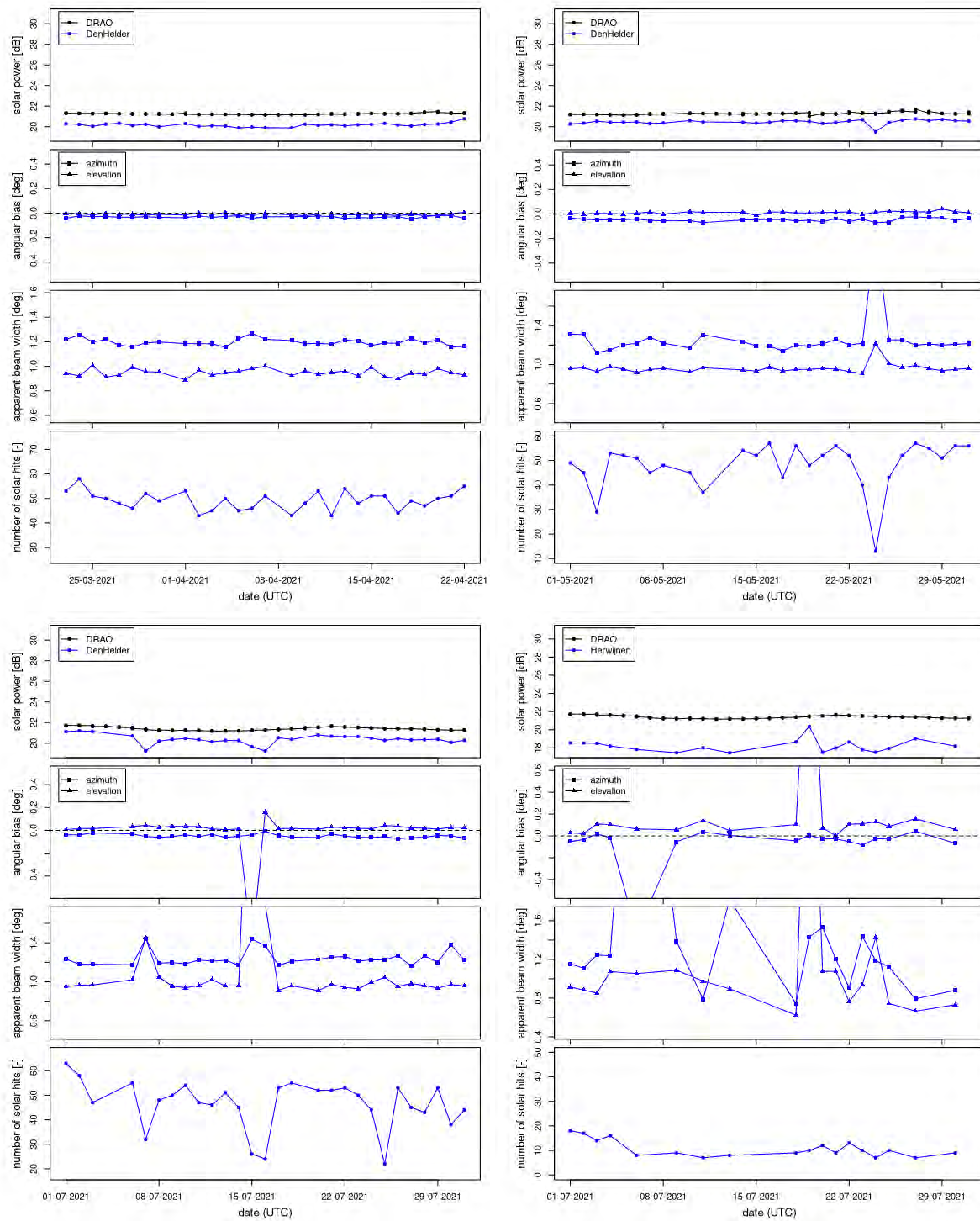


Figure 2.6: Daily time series of elevation and receiver offsets and the estimated and observed solar fluxes. Note that the scale of horizontal and vertical axes is not the same for all graphs. For a fraction of 0.7.

Chapter 3

Design and apply corrections for attenuation by a layer of water on the sphere protecting the radar antenna

3.1 Introduction

An important source of rainfall underestimation for X- or C-band radars is attenuation along the radar beam (Hitschfeld and Bordan, 1954; Tabary et al., 2009). The radar signals especially become weaker when passing through heavy rainfall, leaving less signal to be reflected by precipitation at further range from the radar. The radar reflectivity factors can be corrected for the two-way path-integrated attenuation (Hitschfeld and Bordan, 1954; Carey et al., 2000; Testud et al., 2000; Jacobi and Heistermann, 2016; Overeem et al., 2021). This entails the estimation of the specific attenuation k per range bin, and the integration of k over the entire beam (ray) per azimuth. Next, the horizontally polarised radar reflectivity factor Z is increased by the estimated attenuation.

For dual-pol radars, the so-called specific differential phase (K_{dp}) can be employed to correct for attenuation (Vulpiani et al., 2012; Al-Sakka et al., 2013; Crisologo et al., 2014), which concerns the phase instead of the amplitude of the signals. The value of K_{dp} increases with increasing concentration and drop size. It is immune to attenuation, in contrast to methods that solely rely on Z , and has been shown to outperform such a method, based on a 318-day dataset from the two KNMI radars in the Netherlands (Overeem et al., 2021). A wet radome can lead to signal loss (Ruze, 1965). Hence, rainfall can also be underestimated due to a wet radome, the protective cover of the radar (Germann, 1999; Kurri and Huuskonen, 2008). Precipitation causes a liquid water and/or ice layer on the radome leading to attenuation. Relatively few scientific publications on wet radome attenuation correction have been published, e.g., Gorgucci et al. (2013); Frasier et al. (2013); Van de Beek et al. (2016).

An illustration of the influence of wet radome attenuation on the radar reflectivity factor is provided in Figure 3.1, where four consecutive time intervals are visualised for the KNMI C-band radar in Den Helder (left column) and the KNMI C-band radar in Herwijnen (middle and right columns). The middle column shows the radar reflectivity factor that has been corrected for non-meteorological echoes employing a fuzzy logic algorithm (Overeem et al., 2020) and for rain-induced attenuation along the radar beam employing K_{dp} (Overeem et al., 2021). First, the maps with radar reflectivity factor from the Den Helder (left column) and Herwijnen (right column) radars are compared. For both radars, a similar precipitation pattern is found at 07:45 UTC (first row), but the areas with $Z \geq 7$ dBZ become much smaller and the values for Z become much lower for the Herwijnen radar at 07:50 UTC and to a lesser extent at 07:55 UTC. This coincides with high Z values based on the Den Helder radar over the Herwijnen radar site.

Values for Z and the size of the precipitation areas have clearly increased at 08:00 UTC, for which the Z values from the Den Helder radar above the Herwijnen radar site have decreased. It is difficult to exactly relate values for Z from the Den Helder radar to radome wetting for the Herwijnen radar site, due to the time it takes for rainfall to travel to the Earth's surface, and other representativeness errors (the radar measures aloft and the radar site is at the Earth's surface). Unsurprisingly, at 07:45 UTC already higher values for Z based on the Den Helder radar are present above the Herwijnen radar site. To rule out the possibility that rain-induced attenuation along the radar beam is the main cause of the large reduction in Z values for the Herwijnen radar at 07:45 UTC and 07:50 UTC, the attenuation corrected Z values for the Herwijnen radar are also visualised (middle column)

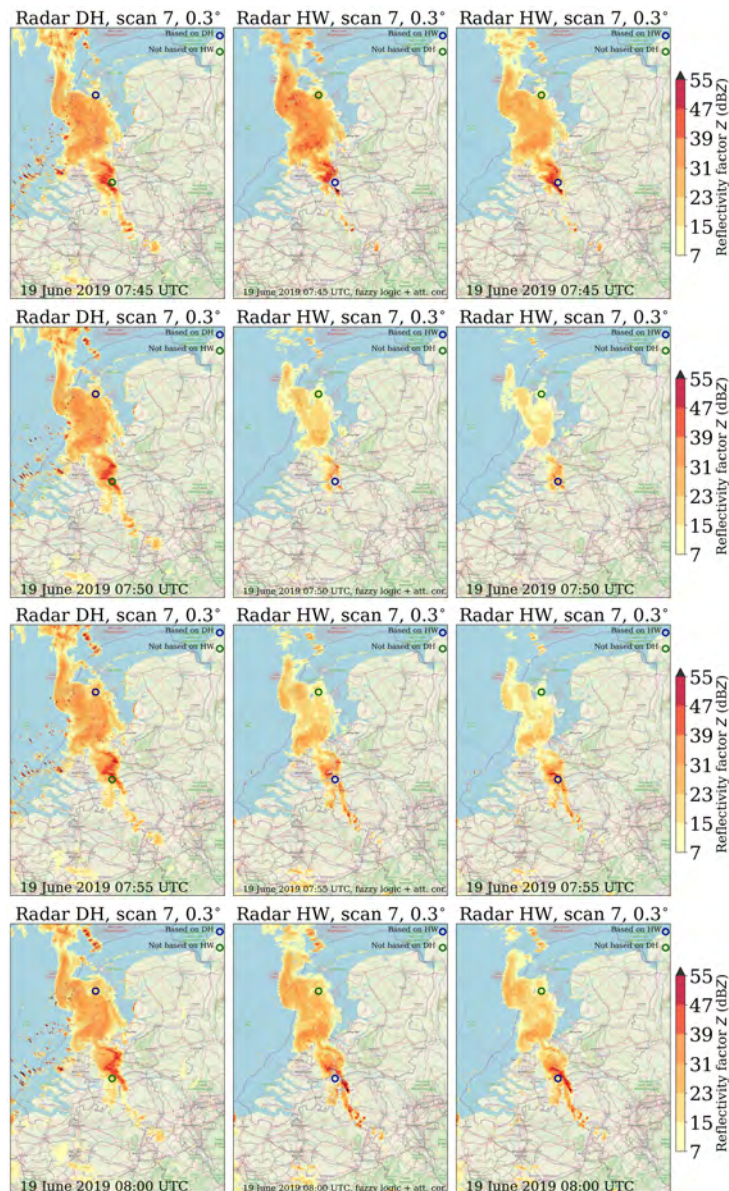


Figure 3.1: An illustration of the impact of wet radome attenuation on the radar reflectivity factor for the KNMI radar in Herwijnen. Radar reflectivity factors are visualised for the Den Helder (left) and the Herwijnen radar (middle, right). The maps in the middle show the results when fuzzy logic non-meteorological echo removal and rain-induced attenuation correction along the radar beam, so not including wet radome attenuation correction, have been applied. Map data ©OpenStreetMap contributors 2023. Distributed under the Open Data Commons Open Database License (ODbL) v1.0.

Although larger values for Z are obtained, there is still a strong reduction in Z . This confirms that wet radome attenuation is likely the main cause for the severe reduction in Z .

3.2 Wet radome attenuation in the literature

Wet radome attenuation is caused by a layer of liquid, melting or solid precipitation. Especially, a mix of liquid water and ice can lead to severe attenuation (Donaldson, 1991; Germann, 1999). Higher rainfall intensities can lead to thicker water layers. The distribution of water on the radome is irregular and depends on precipitation intensity, material of the radome, viscosity of precipitation, radar beam angle, wind direction and wind speed (Germann, 1999). The part of the radome at the windward side is expected to experience more attenuation, especially for higher wind speeds. Usually, a hydrophobic coating is applied to the radome, as is the case for the KNMI radars, which helps to reduce the effect of radome attenuation.

Wet radome attenuation can be assessed by investigating the radar reflectivity factors at the location of an obstacle nearby the radar site, typically within a few kilometres. The close proximity to the radar helps to eliminate other sources of error, such as rain-induced attenuation along the radar beam, as much as possible. The obstacle should be a fixed target. Buildings and metal constructions can result in a high and fairly constant reflectivity, which can act as a reference level. The average signal loss with respect to this reference level is a measure of wet radome attenuation. Leijnse (2012) illustrates the effect of wet radome attenuation for the old KNMI C-band radars in De Bilt and Den Helder, the Netherlands, during the passing of a squall line. The wet radome attenuation is estimated at 4–6 dB, resulting in a decrease of the estimated rainfall intensity by a factor 1.8–2.4. The decrease in reflectivity factor is found by investigating the signal return strength for nearby obstacles: a lighthouse for the Den Helder radar (“Lange Jaap”) and a building for the De Bilt radar. Van de Beek et al. (2016) estimate the wet radome attenuation from the decrease in reflectivity for another event at the location of a large building at 3-km range from the old KNMI C-band radar in De Bilt, the Netherlands. This approach assumes that the influence of rain-induced attenuation along the radar beam, precipitation at the location of the building, and wetting of the building, on the reflectivity are negligible compared to the wet radome attenuation (this also holds for Leijnse (2012)). During dry weather, the average reflectivity is 60 dBZ, with 0.5 dB fluctuations (in this case the level of quantisation of reflectivity). This decreases with 0.5–4 dB during this event with light, moderate and more heavy rainfall. This decrease may be attributed to wet radome attenuation and is employed to increase the reflectivity (Van de Beek et al., 2016).

Germann (1999) analyses five precipitation events for Switzerland, where a highest two-way attenuation of 5.4 dB in reflectivity with a C-band radar is found for a moderate rainfall event. They base their analyses on regions of interest with a size of a few thousands to tens of thousands square kilometres, and investigate time series of reflectivity before, during and after the event. This approach does not investigate the reflectivity by an obstacle.

Merceret and Ward (2002) provide a literature overview of wet radome attenuation estimates and show two-way C-band wet radome losses as a function of rainfall intensity. They provide an empirical equation based on data from Antennas for Communications (AFC) (2002) to compute the two-way transmission loss by wet radome attenuation as a function of microwave frequency, rainfall intensity and hydrophobicity of the radome. This has been incorporated in the open-source Python library wradlib (Heistermann et al., 2013) in function “`atten.correct_radome_attenuation_empirical`” (Wradlib, 2023a). For the C-band (~ 5.6 GHz) radars operating in the Belgian-Dutch-German border region, the wet radome attenuation is estimated at 0.03 dB, 0.30 dB, and 2.97 dB for rainfall intensities of 1 mm h^{-1} , 10 mm h^{-1} , and 100 mm h^{-1} , respectively. The hydrophobicity is determined by an empirical parameter. The implementation in wradlib employs the range bins within a radius from the radar to compute the rainfall intensity at the radome from the reflectivity factor. A limitation of this approach is

that it does not incorporate any azimuthal dependence. Hence, the wet radome attenuation correction is always the same for a given rainfall intensity. It also assumes that the rainfall intensity is accurately known, whereas it is derived from the reflectivity that is influenced by the wet radome attenuation itself.

Others study the effect of wet radome attenuation in laboratory experiments, including the dependence on rainfall intensity and waxing (Kurri and Huuskonen, 2008) or develop an instrument to measure wet radome attenuation (Mancini et al., 2018). One interesting method that makes use of dual-polarisation variables is provided by Gorgucci et al. (2013) for an X-band radar.

Thompson et al. (2012) present a method where the radar acts as a kind of radiometer, from which brightness temperatures are obtained. The higher the brightness temperature, the more severe the attenuation. This approach requires many samples of the raw “IQ” data at far range from the radar, which requires a very slow antenna velocity. At the time of their publication, this method was being implemented for the operational United Kingdom C-band weather radar network. This method cannot be used with the current KNMI radars and is not expected to fit within the scan strategy of the C-band radars in the Belgian-Dutch-German border region.

Here, we explore the detection and quantification of wet radome attenuation by analysing ~ 6 -month time series from the KNMI radars in Herwijnen and Den Helder. For both radars a nearby obstacle is chosen for which the reflectivity values are investigated.

3.3 Results

Reflectivity factor data from both the Herwijnen and Den Helder radars are analysed for a period of 185 days starting on April 1, 2021. In order to observe a possible wet radome effect, only data from the range bins of the lowest elevation scan (0.3 degrees), that are known to hit two tall objects (Figure 3.2), are employed. For the Herwijnen radar, this is the church tower in Zaltbommel (8 km from the radar in east-southeast direction). For the Den Helder radar, the lighthouse Lange Jaap is selected: a tall tower 4 km to the west as seen from the radar.

In line with earlier findings in the literature (Leijnse, 2012; Van de Beek et al., 2016), the initial hypothesis is as follows: the tall object will have a (relatively) constant response in terms of uncorrected reflectivity (uZ). Variations in this response could be due to (1) variations in atmospheric conditions affecting beam propagation - leading to different overlap with the tall objects - and (2) the wet radome effect possibly leading to signal attenuation. In order to find indications for this second effect, the radar reflectivity data at the location of the radar is employed to flag moments when the radome likely got wet due to (heavy) rain.

Radar, rain gauge and wind data were analysed in a Jupyter notebook. Wind was included because it may have considerable impact, especially because for the lowest elevation scan the radar is looking almost horizontally, which is more affected by rain when this is blown against the radome.

Resulting figures are discussed here below. Each figure consists of five panels, each with the same time line. The first displays the radar-derived rain rate R at the radome (taken as the median over a ring of range bins surrounding the radar site), the second displays the uncorrected reflectivity uZ (dBZ) for the selected range bin overlapping with the tall obstacle and for one nearby range bin without such an obstacle (reference range bin). Row three shows the corrected reflectivity, that has undergone Doppler clutter filtering to remove the effect of stationary non-meteorological echoes. Rain gauge observations of a nearby KNMI automatic weather station (1–2 km) are shown on row four. The final row shows wind direction. Different colours represent “all data” (shown in blue for rows 1–4 and in gray for row 5) and events flagged for rain at the radar location. Here, orange indicates events where the radar-derived rain is above the threshold, red indicates when additionally the wind direction at the automatic weather

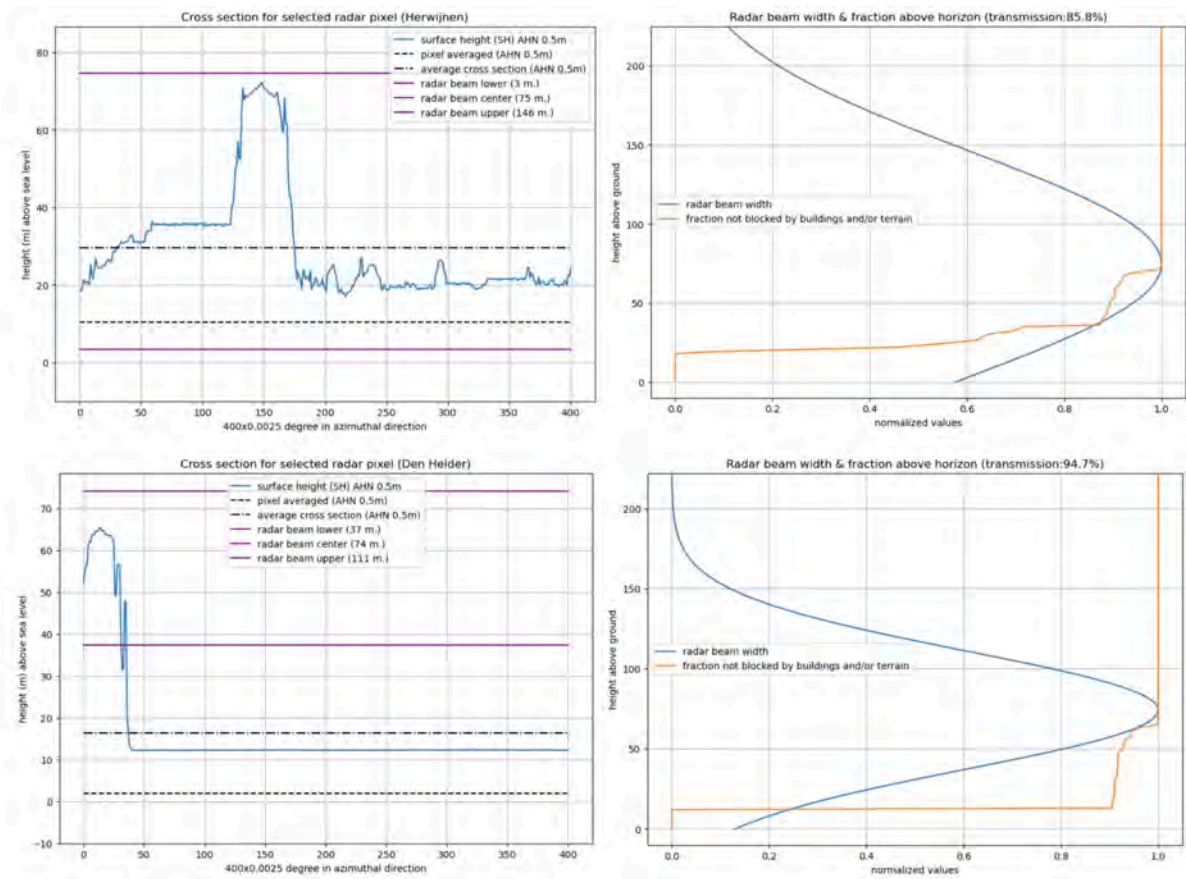


Figure 3.2: Two obstacles close to the KNMI radars: the church tower in Zaltbommel (upper panels; the shape of the tower can be clearly noticed in the left figure) and the lighthouse Lange Jaap (lower panels). Their elevations (left) and the beam blockage (right) have been computed based on the digital elevation model data from AHN4.

station was within the selected intervals. The intervals with a width of 120 degrees in azimuthal direction were chosen such that they are centred in the direction of the tall obstacle as seen from the radar.

First the results for the Herwijnen radar are discussed in Figure 3.3. In order to see evidence for the wet radome effect, the initial focus is on the second row (uZ). Here, the range bin which encompasses the church tower displays a relatively constant and very strong signal at 80 dBZ with every few days a “spike” to lower values (down to $\sim 60 \text{ dBZ}$). These “spikes” do not consist of single observations: when zooming in a gradual decrease of the uZ signal can be seen, followed by a gradual recovery of the signal. This gradual evolution of the spike suggests that it is not related to radar hardware, electronics or software, but rather to atmospheric fluctuations affecting the radar signal. Possibly, some of the spikes are related to anomalous beam propagation: a lower signal in uZ could be due to reduced bending of the radar beam towards the surface, leading to less overlap with the tall object. Rain events are indicated in orange and red in rows one, two, three and five (Figure 3.3). These are identified based on the threshold value for the rain intensity at the radome. Almost none of the spikes in uZ seem to coincide with moments of rain. This observation is quantified by calculating the ratio of uZ for moments with rain (i.e., a wet radome) relative to all moments with no rain (R below the threshold). When this ratio is calculated over the entire period (185 days), it is equal to 1.00. This is based on averaging logarithmic variables and dividing their averages. It is better to first express uZ in $\text{mm}^6 \text{mm}^{-3}$, then compute the average, and then express it in dBZ . Subsequently, the difference in uZ is computed, which yields a $\sim 0.5\text{-dB}$ reduction, which is noticeable. This relative lack of evidence for a wet radome effect led to a further investigation to the impact of combined wind and rain (as explained above). Row five (Figure

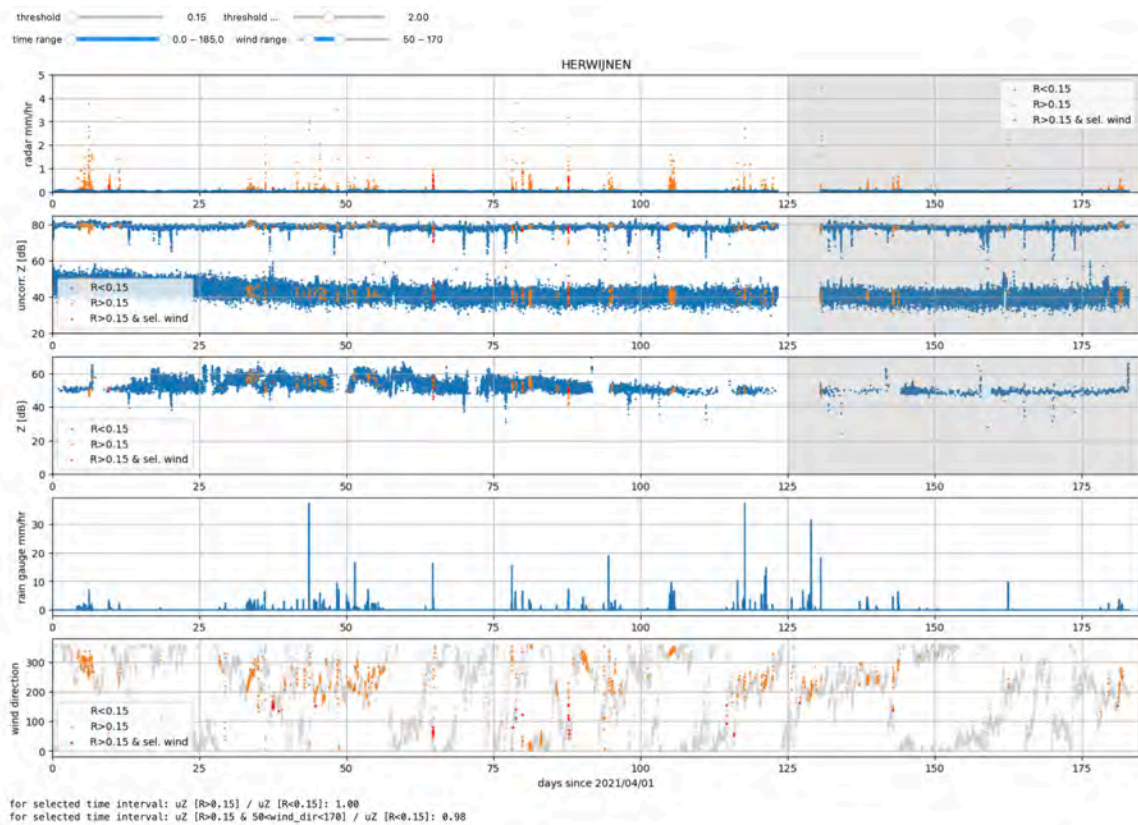


Figure 3.3: Radar-derived rainfall intensity at the radome (row 1), uncorrected (row 2) and corrected (row 3) radar reflectivity factors, rain gauge rainfall intensity (row 4), and wind direction (row 5) for the Herwijnen radar for 185 consecutive days in 2021.

3.3) illustrates in red the moments when not only the rain intensity is above the selected threshold, but also the wind direction is within the selected interval of 120 degrees in azimuthal direction, centred around the direction towards the tall object. When the ratio is calculated for this subset relative to the subset with no rain, a signal reduction of 2% is found in the reflectivity factor (dBZ). More importantly, the decrease in uZ is, on average, ~ 2.7 dB, which is almost 50%.

Figure 3.4 illustrates how a rain event (top row) affects uZ (second row) especially when the wind direction (row five) is within the selected interval. Then, after a sudden change in wind direction (around time 64.75), uZ increases back to its nominal level, despite continuation of rain. It is hypothesised that this rather uncommon combination of wind direction and rain (for Herwijnen most rain comes in from the southwest, whereas the church tower in Zaltbommel is located to the east) explains why only so few similar cases are observed in this period of 185 days.

When comparing the time series for the Den Helder radar (Figure 3.5) with Herwijnen, quite some differences can be observed. Perhaps most striking is the temporal pattern and magnitude (5–15 dB) of fluctuations of the uncorrected reflectivity signal (uZ) relative to a nominal value of 60 dBZ. Again, this could be related to other than normal propagation of the radar beam due to temperature and moisture gradients in the atmosphere, which could be more severe and frequent due to the proximity of the sea. One could imagine that it is related to inaccuracies in the azimuthal or elevation pointing of the radar combined with the relatively narrow size of the object. These strong fluctuations complicate the identification by eye of a wet radome effect (assuming it will have equal magnitude as for Herwijnen: about 2%). The decrease in uZ is, on average, ~ 0.7 dB. However, when the same methodology as for the Herwijnen radar is applied (i.e., selecting a threshold for rain and selecting an interval of wind directions centred around the direction of the tall tower), nevertheless a signal reduction of 3% is found. Then,

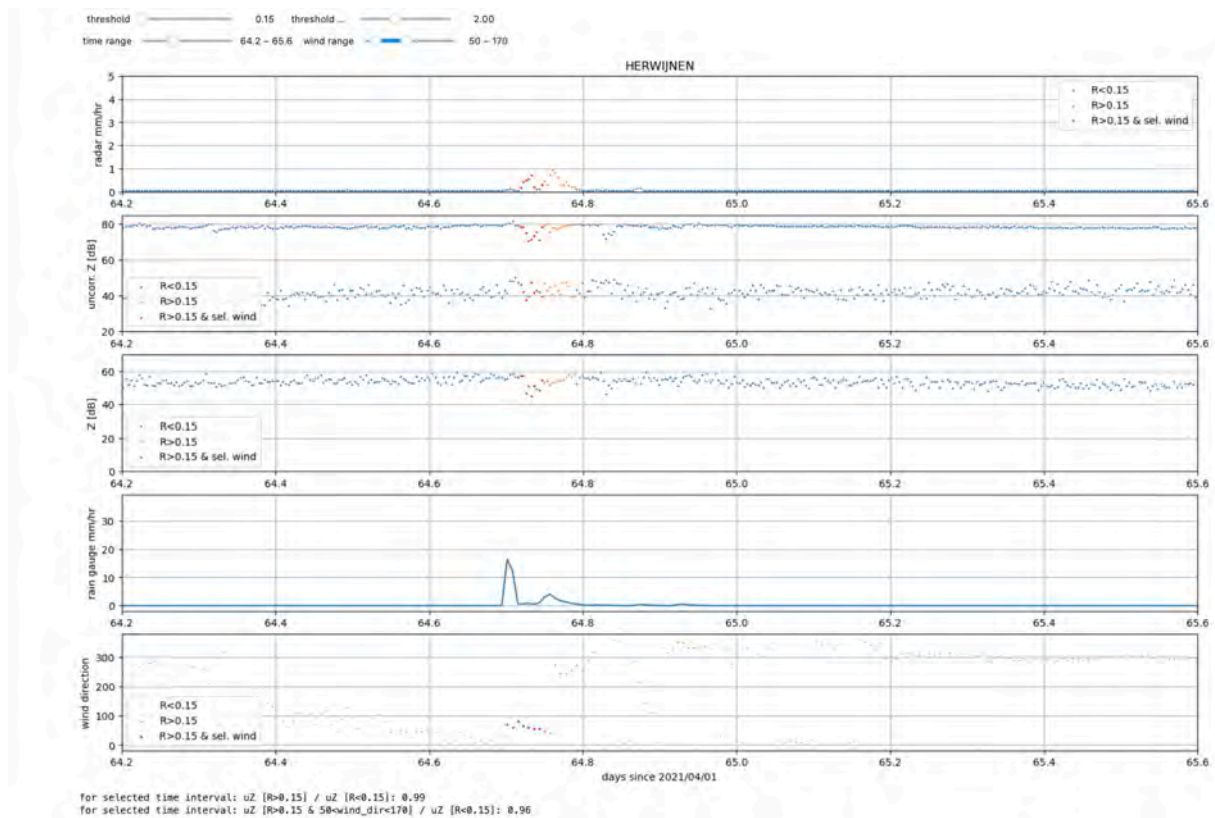


Figure 3.4: Radar-derived rainfall intensity at the radome (row 1), uncorrected (row 2) and corrected (row 3) radar reflectivity factors, rain gauge rainfall intensity (row 4), and wind direction (row 5) for the Herwijnen radar for one event in 2021.

the decrease in uZ is ~ 1.2 dB.

To conclude, wet radome attenuation may have an impact of up to 1.2–2.7 dB reduction of the uncorrected reflectivity, averaged over a ~ 6 -month period. If the effect occurs, then it will have a directional dependence depending on the wind direction at the site of the radar. Further research is needed to further confirm this preliminary conclusion. Amongst others, this research could focus on multiple objects surrounding the radar(s), to investigate the azimuthally dependent wet radome attenuation in relation to wind direction. Another reason for discrepancies could be related to the distance to the chosen obstacles of 4 km and 8 km. Rain-induced attenuation along the radar beam could cause an additional decrease in the uncorrected reflectivity data.

3.4 Conclusions and recommendations

Here, wet radome attenuation has been computed by investigating the decrease in signal level of a nearby obstacle. The fixed-target analyses have provided more insight into wet radome attenuation. On average, a decrease in signal level is found when the radome can be considered wet. This becomes clearer when only data are selected for wind directions that coincide with the azimuth of the obstacle as seen from the radome. Still, in many cases the reflectivity at the fixed target decreases when the radome is not wet or remains fairly constant when the radome should be wet. This may be related to other than normal propagation conditions of the radar signal, causing the radar signal to (partially) miss the fixed target. Here, beam propagation modelling could help to identify the data points with normal propagation (see recommendations in Chapter 1 how to achieve this). Analyses of longer datasets would




Figure 3.5: Radar-derived rainfall intensity at the radome (row 1), uncorrected (row 2) and corrected (row 3) radar reflectivity factors, rain gauge rainfall intensity (row 4), and wind direction (row 5) for the Den Helder radar for 185 consecutive days in 2021.

allow for better characterisation of the influence of wind direction, and also allow for an evaluation as a function of wind speed.

Wet radome attenuation is expected to vary considerably with azimuth. Given the lack of stable reflections of buildings, the azimuthally varying wet radome attenuation will be difficult to quantify (Leijnse, 2012). To conclude, a wet radome attenuation correction based on fixed-target returns will be difficult to incorporate in a (real-time) correction of radar precipitation products.

Developing a wet radome attenuation correction algorithm is a highly innovative research topic. Challenges encompass the irregular distribution of a water layer on the radome, dependence on the precipitation type (e.g., mixed precipitation), finding a robust method, and degradation of the hydrophobic coating in time. Though a few wet radome attenuation correction algorithms have been proposed in the literature, it seems not common practice to apply such a correction. We provide the following recommendations:

- More literature study and discussions with colleagues from other national meteorological services to obtain a better overview of possibly available wet radome attenuation correction algorithms or to identify the existence of the application of such algorithms in radar precipitation products.
- Gorgucci et al. (2013) estimate the wet radome attenuation for an X-band radar and Le Loh et al. (2022) for S- and C-band radars, employing the so-called self-consistency relationship taking advantage of the reflectivity factor and the dual-polarisation variables differential reflectivity and specific differential phase (K_{dp}). The latter is immune for radome attenuation. This approach



seems promising and could be explored in a future study. Such a method could also be employed to estimate reflectivity biases caused by radar miscalibration (Le Loh et al., 2022) (Chapter 2).

- K_{dp} could be used directly to estimate rainfall intensity. This can only be reliably applied in case of liquid precipitation and moderate to heavy rainfall as indicated by the value of the radar reflectivity factor. These conditions will not always be met, especially at longer range from a radar, where the radar beam may only experience solid precipitation. These moderate to heavy rainfall events are the ones that result in the highest wet radome attenuation, whereas rainfall estimates obtained from K_{dp} are not affected by wet radome attenuation. An example of rainfall estimation employing K_{dp} and employing Z (that has undergone fuzzy logic non-meteorological echo removal and rain-induced attenuation correction along the radar beam) is provided in figure 3.6 for 14 July 2021, and was obtained from another project (“beleidstafel wateroverlast en hoogwater”) where this algorithms has extensively been investigated. For one automatic rain gauge location, the radar-based 1-h rainfall estimates from those methods are compared to the 1-h rain gauge accumulations. For this particular event, the rainfall estimates based on K_{dp} are (much) better for the radars in Essen, Herwijnen, and Houthalen-Helchteren (three time series plots on the left in the bottom panel).

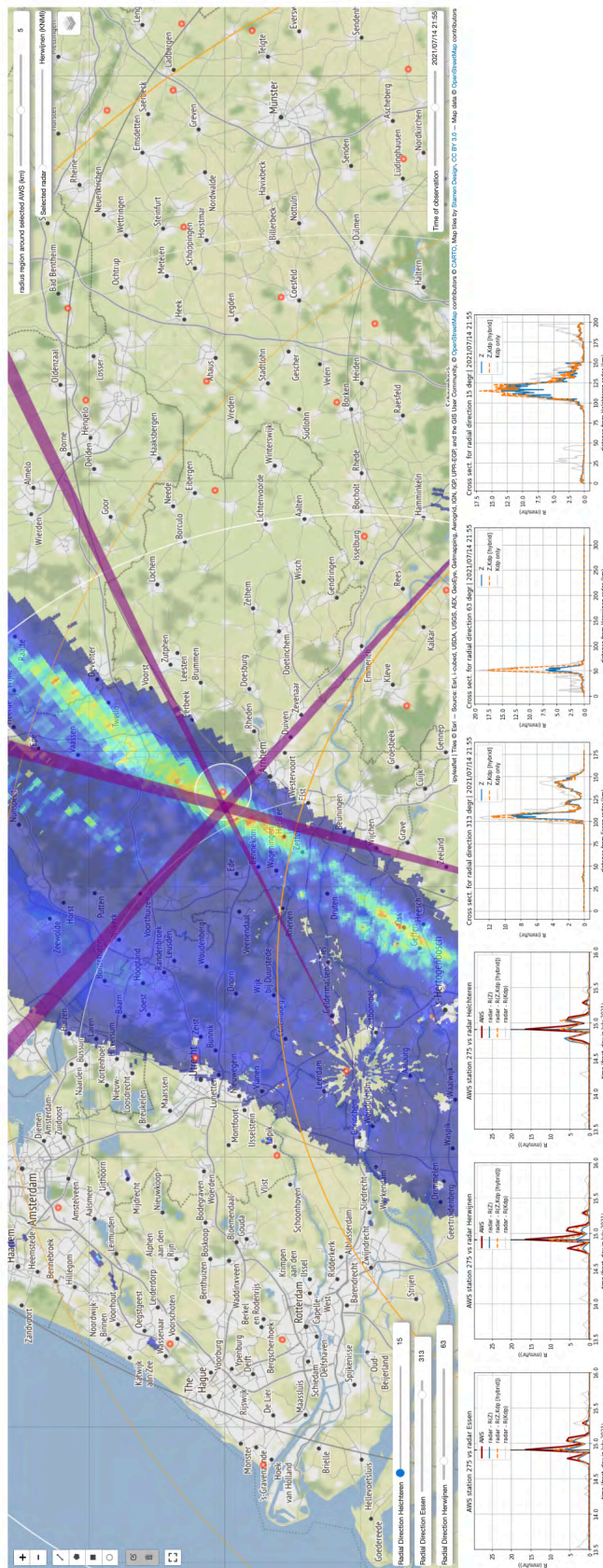


Figure 3.6: Screenshot of the so-called radar research dashboard for a precipitation event on 14 July 2021. The purple lines show the radar beam for the lowest elevation scan from the radars in Essen, Herwijnen, and Houthalen-Helchteren. The red dot enclosed by a white circle indicates the location of the rain gauge.



Acknowledgements


Maps were produced with Python package Cartopy. (Met Office, 2022).

Bibliography

- Al-Sakka H, Boumahmoud AA, Fradon B, Frasier SJ, Tabary P. A new fuzzy logic hydrometeor classification scheme applied to the French X-, C-, and S-band polarimetric radars. *J Appl Meteor Climatol* 2013;52(10):2328–2344.
- Antennas for Communications (AFC), AFC's radome hydrophobic surfaces; 2002. <https://www.radome.net/hydropho.html>, retrieved October 2023.
- Bech J, Codina B, Lorente J, Bebbington D. The sensitivity of single polarization weather radar beam blockage correction to variability in the vertical refractivity gradient. *J Atmos Oceanic Technol* 2003;20(6):845–855.
- Bech J, Gjertsen U, Haase G. Modelling weather radar beam propagation and topographical blockage at northern high latitudes. *Quart J Roy Meteor Soc* 2007;133:1191–1204.
- Van de Beek CZ, Leijnse H, Hazenberg P, Uijlenhoet R. Close-range radar rainfall estimation and error analysis. *Atmos Meas Tech* 2016;9:3837–3850.
- Beekhuis H, Mathijssen T. From pulse to product, Highlights of the upgrade project of the Dutch national weather radar network. In: de Vos L, Leijnse H, Uijlenhoet R, editors. 10th European Conference on Radar in Meteorology and Hydrology (ERAD 2018): 1-6 July 2018, Ede-Wageningen, The Netherlands Wageningen University & Research, Wageningen, the Netherlands; 2018.p. 960–965.
- Belmonte A, Fabregas X. Analysis of wind turbines blockage on Doppler weather radar beams. *IEEE Antennas and Wireless Propagation Letters* 2010;9:670–673.
- Carey LD, Rutledge SA, Ahijevych DA, Keenan TD. Correcting propagation effects in C-band polarimetric radar observations of tropical convection using differential propagation phase. *J Appl Meteor* 2000;39(9):1405–1433.
- Cremonini R, Moisseev D, Chandrasekar V. Airborne laser scan data: a valuable tool with which to infer weather radar partial beam blockage in urban environments. *Atmos Meas Tech* 2016;9:5063–5075.
- Crisologo I, Vulpiani G, Abon CC, David CPC, Bronstert A, Heistermann M. Polarimetric rainfall retrieval from a C-band weather radar in a tropical environment (the Philippines). *Asia-Pac J Atmos Sci* 2014;50(S):43–55.
- Donaldson NR. An example of attenuation by wet snow on a radar dome. *Atmosphere-Ocean* 1991;29(4):699–711.
- Fabry F, Frush C, Zawadzki I, Kilambi A. On the extraction of near-surface index of refraction using radar phase measurements from ground targets. *J Atmos Oceanic Technol* 1997;14:978–987.
- Farr TG, *et al* . The Shuttle Radar Topography Mission. *Rev Geophys* 2007;45. RG2004.
- Farr TG, Kozub M. Shuttle Radar Topography Mission produces a wealth of data. *Eos Trans AGU* 2000;81:583–583.

- Frasier SJ, Kabeche F, Figueras i Ventura J, Al-Sakka H, Tabary P, Beck J, et al. In-place estimation of wet radome attenuation at X Band. *J Atmos Oceanic Technol* 2013;30:917–928.
- Frech M, Hagen M, Mammen T. Monitoring the absolute calibration of a polarimetric weather radar. *J Atmos Oceanic Technol* 2017;34(3):599–615.
- Germann U. Radome attenuation — a serious limiting factor for quantitative radar measurements? *Meteor Z* 1999;8(3):85–90.
- Gorgucci E, Bechini R, Baldini L, Cremonini R, Chandrasekar V. The influence of antenna radome on weather radar calibration and its real-time assessment. *J Atmos Oceanic Technol* 2013;30:676–689.
- Heistermann M, Jacobi S, Pfaff T. Technical Note: An open source library for processing weather radar data (*wradlib*). *Hydrol Earth Syst Sci* 2013;17:863–871.
- Hitschfeld W, Bordan J. Errors inherent in the radar measurement of rainfall at attenuating wavelengths. *J Meteor* 1954;11(1):58–67.
- Holleman I, Beekhuis H, *Weather radar monitoring using the sun*; 2004. Technical report TR-272, KNMI, De Bilt, available via https://cdn.knmi.nl/system/data_center_publications/files/000/066/270/original/tr_suncalibration.pdf?1495620525.
- Holleman I, Huuskonen A, Taylor B. Solar monitoring of the NEXRAD WSR-88D network using operational scan data. *J Atmos Oceanic Technol* 2022;39:193–205.
- Huuskonen A, Holleman I. Determining weather radar antenna pointing using signals detected from the sun at low antenna elevations. *J Atmos Oceanic Technol* 2007;24:476–483.
- Huuskonen A, Kurri M, Hohti H, Beekhuis H, Leijnse H, Holleman I. Radar performance monitoring using the angular width of the solar image. *J Atmos Oceanic Technol* 2014;31:1704–1712.
- Jacobi S, Heistermann M. Benchmarking attenuation correction procedures for six years of single-polarized C-band weather radar observations in South-West Germany. *Geomat Nat Haz Risk* 2016;7(6):1785–1799.
- Kobrick M. On the toes of giants—How SRTM was born. *Photogramm Eng Remote Sens* 2006;72:206–210.
- Krajewski WF, Ntelekos AA, Goska R. A GIS-based methodology for the assessment of weather radar beam blockage in mountainous regions: two examples from the US NEXRAD network. *Computers & Geosciences* 2006;32:283–302.
- Kurri M, Huuskonen A. Measurements of the transmission loss of a radome at different rain intensities. *J Atmos Oceanic Technol* 2008;25:1590–1599.
- Lang TJ, Nesbitt SW, Carey LD. On the correction of partial beam blockage in polarimetric radar data. *J Atmos Oceanic Technol* 2009;26:943–957.
- Le Loh J, Chang W, Hsu H, Lin P, Chang P, Teng Y, et al. Long-term assessment of the reflectivity biases and wet-radome effect using collocated operational S- and C-band dual-polarization radars. *IEEE Transactions on Geoscience and Remote Sensing* 2022;60:1–17.
- Leijnse H. Verdwijvende regenbuien. *Nederlands Tijdschrift voor Natuurkunde* 2012;78(3):92–93.
- Leijnse H, Teschl R, Paulitsch H, Teschl F, Holmes G, Sidselrud LF, *OPERA-4: On the coexistence of weather radars and wind turbines*; 2022. EUMETNET, OPERA, available via https://www.eumetnet.eu/wp-content/uploads/2022/08/OPERA_wind_turbine_report_20220225.pdf.

- Mancini A, Salazar JL, Lebrón RM, Cheong BL. A novel instrument for real-time measurement of attenuation of weather radar radome including its outer surface. Part I: The concept. *J Atmos Oceanic Technol* 2018;35:953–973.
- McRoberts DB, Nielsen-Gammon JW. Detecting beam blockage in radar-based precipitation estimates. *J Atmos Oceanic Technol* 2017;34:1407–1422.
- Merceret FJ, Ward JG. Attenuation of weather radar signals due to wetting of the radome by rainwater or incomplete filling of the beam Volume; 2002. National Aeronautics and Space Administration, Kennedy Space Center, FL United States, April 2020, NASA/TM-2002-211171. Available via <https://ntrs.nasa.gov/search.jsp?R=20020043890>.
- Met Office, Cartopy: A cartographic python library with a Matplotlib interface. Exeter, Devon; 2022. <https://scitools.org.uk/cartopy>.
- Mühlbauer K, Goudenhoofd E, Heistermann M, Helmus JJ, Guy N, Pfaff T, et al., wradlib/wradlib: wradlib release v1.19.2 (1.19.2). Zenodo. Zenodo; 2023.
- NASA, Shuttle Radar Topography Mission (SRTM) Global. Distributed by OpenTopography; 2013. <https://doi.org/10.5069/G9445JDF>.
- Overeem A, Holleman I, Buishand A. Derivation of a 10-year radar-based climatology of rainfall. *J Appl Meteor Climatol* 2009;48:1448–1463.
- Overeem A, Uijlenhoet R, Leijnse H. Full-year evaluation of non-meteorological echo removal with dual-polarization fuzzy logic for two C-band radars in a temperate climate. *J Atmos Oceanic Technol* 2020;37(9):1643–1660.
- Overeem A, de Vries H, Al Sakka H, Uijlenhoet R, Leijnse H. Rainfall-induced attenuation correction for two operational dual-polarization C-band radars in the Netherlands. *J Atmos Oceanic Technol* 2021;38(6):1125–1142.
- Rosen PA, et al. Synthetic aperture radar interferometry. *Proc IEEE* 2000;88:333–382.
- Ruze J. More on wet radomes. *IEEE Transactions on Antennas and Propagation* 1965;13(5):823–824.
- SIGMET, *RVP6 Doppler signal processor user's manual*; 1998. SIGMET, 208 pp. Available from SIGMET, Inc., 2 Park Drive, Westford, MA 01886.
- Steiner M, Smith JA. Use of three-dimensional reflectivity structure for automated detection and removal of nonprecipitating echoes in radar data. *J Atmos Oceanic Technol* 2002;19:673–686.
- Tabary P, Vulpiani G, Gourley JJ, Illingworth AJ, Thompson RJ, Bousquet O. Unusually high differential attenuation at C Band: Results from a two-year analysis of the French Trappes polarimetric radar data. *J Appl Meteor Climatol* 2009;48(10):2037–2053.
- Testud J, Le Bouar E, Obligis E, Ali-Mehenni M. The rain profiling algorithm applied to polarimetric weather radar. *J Atmos Oceanic Technol* 2000;17(3):332–356.
- Thompson R, Illingworth A, Ovens J. Emission: a simple new technique to correct rainfall estimates from attenuation due to both the radome and heavy rainfall. In: Moore RJ, Cole SJ, Illingworth AJ, editors. *Weather Radar and Hydrology, Proceedings of a symposium held in Exeter, UK, April 2011 IAHS Publ. 351*, IAHS Press, Wallingford, Oxfordshire, U.K.; 2012.p. 39–44.
- Vulpiani G, Montopoli M, Passeri LD, Gioia AG, Giordano P, Marzano FS. On the use of dual-polarized C-band radar for operational rainfall retrieval in mountainous areas. *J Appl Meteor Climatol* 2012;51:405–425.



Wradlib, wradlib atten.correct_radome_attenuation_empirical; 2023. https://docs.wradlib.org/en/stable/generated/wradlib.atten.correct_radome_attenuation_empirical.html, retrieved October 2023.

Wradlib, wradlib.qual.beam_block_fr - wradlib; 2023. https://docs.wradlib.org/en/latest/generated/wradlib.qual.beam_block_frac.html, retrieved October 2023.

Zhang P, Zrnić D, Ryzhkov A. Partial beam blockage correction using polarimetric radar measurements. *J Atmos Oceanic Technol* 2013;30(5):861-872.